

# THE NUCLEOSYNTHESIS OF $^{26}\text{Al}$ AND $^{60}\text{Fe}$ IN SOLAR METALLICITY STARS EXTENDING IN MASS FROM 11 TO 120 $M_{\odot}$ : THE HYDROSTATIC AND EXPLOSIVE CONTRIBUTIONS

MARCO LIMONGI<sup>1,2</sup> AND ALESSANDRO CHIEFFI<sup>2,3</sup>

Received 2006 February 10; accepted 2006 April 11

## ABSTRACT

We present the  $^{26}\text{Al}$  and  $^{60}\text{Fe}$  yields produced by a generation of solar metallicity stars ranging in mass between 11 and 120  $M_{\odot}$ . We discuss the production sites of these  $\gamma$ -ray emitters and quantify the relative contributions of the various components. We provide the contributions of the wind, the C convective shell, and the explosive Ne/C burning to the total  $^{26}\text{Al}$  yield together with the contributions of the He convective shell, the C convective shell, and the explosive Ne/C burning to the  $^{60}\text{Fe}$  yield. We conclude that, at variance with current beliefs,  $^{26}\text{Al}$  is mainly produced by the explosive C/Ne burning over most of the mass interval analyzed here, while  $^{60}\text{Fe}$  is mainly produced by the C convective shell and the He convective shell. By means of these yields we try to reproduce two quite strong observational constraints related to the abundances of these nuclei in the interstellar medium, i.e., the number of  $\gamma_{1.8}$  photons per Lyman continuum photon,  $R_{\text{GXL}}$ , and the  $^{60}\text{Fe}/^{26}\text{Al}$   $\gamma$ -ray line flux ratio.  $R_{\text{GXL}}$  is found to be roughly constant along the Galactic plane (and of the order of  $1.25 \times 10^{-11}$ ), while the  $^{60}\text{Fe}/^{26}\text{Al}$  ratio has been recently measured by both *RHESSI* ( $0.17 \pm 0.05$ ) and SPI (*INTEGRAL*) ( $0.11 \pm 0.03$ ). We can quite successfully fit simultaneously both ratios for a quite large range of exponents of the power-law initial mass function. We also address the fit to  $\gamma^2$  Velorum, and we find that a quite large range of initial masses, at least from 40 to 60  $M_{\odot}$ , do eject an amount of  $^{26}\text{Al}$  (through the wind) compatible with the current upper limit quoted for this W-R star: such a result removes a long-standing discrepancy between the models and the observational data.

*Subject heading:* gamma rays: theory — nuclear reactions, nucleosynthesis, abundances — stars: evolution — supernovae: general

*Online material:* color figures, machine-readable table

## 1. INTRODUCTION

The quest for the main  $^{26}\text{Al}$  source(s) started as soon as the first observational evidence of the presence of live  $^{26}\text{Al}$  in the inner Galaxy was demonstrated by the *HEAO-3* experiment (Mahoney et al. 1982, 1984), and it still continues to the present day. Its presence in the interstellar medium was not a surprise because it was theoretically predicted since the middle of the 1970s that explosive Ne/C burning in core-collapse supernovae may produce such a nucleus (Arnett 1977; Ramaty & Lingenfelter 1977; Truran & Cameron 1978; Arnett & Wefel 1978; Woosley & Weaver 1980). Later on, Dearborn & Blake (1985) pointed out that  $^{26}\text{Al}$  may be injected into the interstellar medium also by Wolf-Rayet (W-R) stars through stellar wind, and since then a number of works have been devoted to the prediction of the amount of  $^{26}\text{Al}$  ejected by these stars (e.g., Prantzos & Casse 1986; Walter & Maeder 1989; Meynet et al. 1997; Vuissoz et al. 2004; Palacios et al. 2005). Arnould et al. (1980) and Clayton (1984), on the basis of the theoretical models available at that time, also proposed the novae as main  $^{26}\text{Al}$  producers. All these candidates, with the further addition of the asymptotic giant branch stars (Mowlavi & Meynet 2000), could in principle account for a significant fraction of the observed flux due to the uncertainties in both the frequencies of the various candidates and the yields itself. Leising & Clayton (1985) were the

first to point out that the lack of information about the distribution of the  $^{26}\text{Al}$  in the Galaxy severely limits the possibility of identifying the main  $^{26}\text{Al}$  donor(s). A clear snapshot of the situation just before the launch of the *Compton Gamma Ray Observatory* (*CGRO*) is provided by the Prantzos (1991) review paper.

The launch of the *CGRO* in 1991, and its continuous operation up to 2001, allowed the first mapping of the 1809 keV line all over the Galaxy and put firm constraints on the possible main sources of  $^{26}\text{Al}$ . By the way, the latest all-sky map has been published by Plüschke et al. (2001). This observational campaign showed beyond any doubt that the  $^{26}\text{Al}$  distribution was strongly confined toward the Galactic disk and quite clumpy and asymmetric, strongly pushing toward a massive star parent for the bulk of the  $^{26}\text{Al}$ . We refer the reader to the reviews by Prantzos & Diehl (1996) and Diehl & Timmes (1998) for an excellent, clear picture of the scenarios that were under debate as soon as the first results from COMPTEL aboard the *CGRO* became available. A further milestone progress in the identification of the main  $^{26}\text{Al}$  producers was obtained when the  $^{26}\text{Al}$  map was compared to a series of all sky maps obtained at various wavelengths. Knödseder et al. (1999) and Knödseder (1999) found that the 53 GHz microwave free-free emission all-sky map was the only one to almost perfectly overlap the  $^{26}\text{Al}$  all-sky map. The 53 GHz free-free emission line maps the regions of ionized gas and such a sustained ionization may be powered only by the Lyman continuum photons provided by the very massive stars and disappears on a timescale of 1 Myr after the switch off of the Lyman continuum "lamp." Hence the existence of such a good overlap between the two all-sky maps demonstrates beyond any reasonable doubt that the bulk of the  $^{26}\text{Al}$  is produced in the same regions where massive stars are present. Such a finding did not at all close the quest of the  $^{26}\text{Al}$  progenitors

<sup>1</sup> Istituto Nazionale di Astrofisica-Osservatorio Astronomico di Roma, Via Frascati 33, I-00040, Monteporzio Catone, Italy; marco@oa-roma.inaf.it.

<sup>2</sup> Centre for Stellar and Planetary Astrophysics, School of Mathematical Sciences, P.O. Box, 28M, Monash University, Victoria 3800, Australia.

<sup>3</sup> Istituto Nazionale di Astrofisica-Istituto di Astrofisica Spaziale e Fisica Cosmica, Via Fosso del Cavaliere, I-00133, Roma, Italy; alessandro.chieffi@iasf-roma.inaf.it.

but simply shifted such a quest toward which subclass of massive stars do mainly contribute to the  $^{26}\text{Al}$  budget. The two classical competing candidates were identified as the Type II supernovae and the W-R stars (through the stellar wind). A further question concerned the possibility, sometimes suggested, that a consistent fraction of the 1.8 MeV  $\gamma$ -flux ( $\gamma_{1.8}$ ) was due to close localized sources and not to Galaxy-wide sources. Such a doubt was mainly due to the fact that the massive star census in the Galaxy is well known only out to distances of a few kiloparsecs and many regions of the Galaxy are obscured for direct measurements. This problem was recently definitely solved by SPI (Spectrometer for *INTEGRAL*; Diehl et al. 2006), which measured for the first time with great accuracy the Doppler shift of the  $^{26}\text{Al}$  line along the inner Galaxy, clearly demonstrating that the  $^{26}\text{Al}$  corotates with the Galaxy, hence supporting a Galaxy-wide origin. The total amount of  $^{26}\text{Al}$  present in the disk of our Galaxy has been estimated by assuming a variety of distributions of the  $^{26}\text{Al}$  sources, and it ranges between 1 and 3  $M_{\odot}$ .

Together with the search for a signal from the decay of  $^{26}\text{Al}$ , a signal from another  $\gamma$ -ray emitter, namely,  $^{60}\text{Fe}$ , has also been searched for thoroughly. The production of this nucleus has been historically attributed to the Ne explosive burning in core-collapse supernovae (Clayton 1982); hence it has always been considered as the litmus test to discriminate among the various candidates as major  $^{26}\text{Al}$  contributors. Unfortunately, all the experiments up to 2002 could only provide upper limits on the abundance of this nucleus in the interstellar medium. With the launch of the *Reuven Ramaty High Energy Solar Spectroscopic Imager* (*RHESSI*) and the *International Gamma-Ray Astrophysics Laboratory* (*INTEGRAL*) the situation changed drastically, since both *RHESSI* and SPI aboard *INTEGRAL* were able to measure an  $^{60}\text{Fe}$  signal from the inner radiant of our Galaxy. The latest simultaneous measurements of  $^{26}\text{Al}$  and  $^{60}\text{Fe}$  performed by *RHESSI* and SPI at the time of writing give  $^{60}\text{Fe}/^{26}\text{Al}$   $\gamma$ -ray line flux ratios equal to  $0.17 \pm 0.05$  (Smith 2006) and  $0.11 \pm 0.03$  (Harris et al. 2005), respectively.

The theoretical models that constitute the base of the various interpretations of these data may be divided in two broad categories: the first one includes stars less massive than, say, 35–40  $M_{\odot}$ , and the second one includes more massive stars. This limiting mass roughly marks the minimum mass that becomes a W-R star. The evolution of the stars in the first group has been extensively explored through all the hydrostatic burnings up to the core collapse together with the following explosive burnings. Yields for both  $^{26}\text{Al}$  and  $^{60}\text{Fe}$  have been published for this mass range over the years by several groups (Woosley & Weaver 1995, hereafter WW95; Thielemann et al. 1996; Rauscher et al. 2002; Limongi & Chieffi 2003; Chieffi & Limongi 2004). The evolution of the stars in the upper mass range, which spend part of their lifetime as W-R stars, has never been followed all along their full evolution (and final explosion), but only through the H- and He-burning (plus, quite recently, the central C-burning) phases; obviously the explosive burnings of these very massive stars have never been addressed either. As a consequence of this very biased knowledge of the evolution of these very massive stars, only the fraction of  $^{26}\text{Al}$  yield ejected by the stellar wind has been predicted up to now (e.g., Prantzos et al. 1986a, 1986b; Walter & Maeder 1989; Meynet et al. 1997; Palacios et al. 2005), and unfortunately quite often this partial prediction has been interpreted as the total  $^{26}\text{Al}$  yield produced by these very massive stars. In other words, it has become a deep-seated notion that the stars that do not become W-Rs contribute to both the  $^{26}\text{Al}$  and  $^{60}\text{Fe}$  yields, while those that become W-Rs contribute only to the synthesis of the  $^{26}\text{Al}$ . Within this accepted framework, an “observed”  $^{60}\text{Fe}/^{26}\text{Al}$  flux ratio of 0.11–0.17 would favor the masses that do not become W-Rs as the

main producers of both  $^{26}\text{Al}$  and  $^{60}\text{Fe}$  (Timmes et al. 1995). Indeed, the WW95 models do predict a  $^{60}\text{Fe}/^{26}\text{Al}$  flux ratio of 0.18 (averaged over a power law,  $\text{IMF}-dn/dm = M^{(-2.35)}$ , ranging between 11 and 40  $M_{\odot}$ ). However, more recent models (Rauscher et al. 2002; Limongi & Chieffi 2003; Chieffi & Limongi 2004) do predict much larger  $^{60}\text{Fe}/^{26}\text{Al}$  flux ratios (0.5–1.0), leaving therefore plenty of room for an important contribution of the W-R stars to the synthesis of the  $^{26}\text{Al}$  (Prantzos 2004). For sake of completeness, it must be mentioned that Woosley et al. (1995) published the presupernova evolution and explosive yields of massive pure He cores that should be associated to W-R stars. However, unfortunately, these bare cores can hardly be reconciled with a population of (single) W-R stars because all of them correspond to models that lose the H-rich mantle before the central He ignition, while consistent models of massive stars with mass loss (see below) show that this happens only in stars more massive than 80  $M_{\odot}$ .

In this paper we completely reanalyze and rediscuss the interpretation of the observed fluxes of both  $^{26}\text{Al}$  and  $^{60}\text{Fe}$  in the light of a new large grid of massive star models of solar metallicity with mass loss. These homogeneous sets of models extend in mass between 11 and 120  $M_{\odot}$  and cover the full hydrostatic evolution from the main sequence up to the core collapse together with the following explosive burnings. These models will be published shortly. Given the importance of the problems connected with the  $\gamma$ -ray emitters  $^{26}\text{Al}$  and  $^{60}\text{Fe}$ , we think that it is worth dedicating a full paper to them. We are aware that these models are just solar metallicity models and that it would be important to have super-solar models too, but we think that the availability of a full set of models from 11 to 120  $M_{\odot}$  covering all the hydrostatic and explosive burnings is already a big step forward in the understanding of these nuclei. We also address the fit to  $\gamma^2$  Velorum, the closest W-R star.

The paper is organized as follows. First, the new set of models is briefly presented, and then two distinct sections discuss separately the theoretical yields of these two nuclei as a function of the initial mass. Their dependence on the mass-loss rate adopted in the WNE+WCO phase is addressed in § 5. A discussion of the scenarios that comes out from the adoption of these new yields and a final brief conclusion follow.

## 2. THE STELLAR MODELS

The  $^{26}\text{Al}$  and  $^{60}\text{Fe}$  yields used in the present paper have been extracted from a new generation of stellar models that will be available soon. These new models have been computed with the latest release (5.050218) of the FRANEC (Frascati Raphson Newton Evolutionary Code). By the way, from now on the release number will follow the following convention: the integer part of the number refers to the major release (the fifth at present), while its decimal part refers to the date on which it has been released, in the form YYMMDD. The main features of this new release, with respect to that described in Limongi & Chieffi (2003), are the following. First of all, the convective mixing and the nuclear burning are coupled together and solved simultaneously. More specifically, the set of equations describing the chemical evolution of the matter are now

$$\frac{dY_i}{dt} = \left( \frac{\partial Y_i}{\partial t} \right)_{\text{nuc}} + \frac{\partial}{\partial m} \left[ (4\pi r^2 \rho)^2 D \frac{\partial Y_i}{\partial m} \right],$$

where the diffusion coefficient  $D$  is given by  $D = 1/3 v_c l$ , the convective velocity  $v_c$  is computed by means of the mixing length theory, and  $l$  is the mixing length parameter. This set of

TABLE 1  
NETWORK REFERENCE MATRIX

Isotope	(p, γ)	(p, α)	(p, n)	(α, γ)	(α, p)	(α, n)	(n, γ)	(n, p)	(n, α)	(γ, p)	(γ, α)	(γ, n)	(β <sup>+</sup> )	(β <sup>-</sup> )
N.....	BK													OD94
H1.....	NACR												OD94	
H2.....	NACR			NACR			FKTH							
H3.....	CA88		CA88	NACR		CA88								RATH
He3.....	FKTH			NACR	NACR		FKTH	CA88						
He4.....					NACR	FKTH								
Li6.....	NACR	NACR		CA88	NACR		FKTH		CA88					
Li7.....		NACR	CA88	NACR	FKTH	NACR	BK							
Be7.....		NACR		NACR	NACR			CA88	FKTH					
Be9.....	NACR	NACR			FKTH	NACR	FKTH		FKTH					

NOTES.—BK = Bao et al. (2000). BKRT = Bao et al. (2000) in the energy range 5–100 keV and Rauscher & Thielemann (2000) above this limit, but rescaled to match the experimental values of Bao et al. (2000) at 100 keV. CA88 = Caughlan & Fowler (1988). FKTH = Thielemann et al. (1996), the Reaction Rate Library REACLIB, in which the experimental values are preferred whenever available (for experimental rates the references are reported in the library). IL01 = Iliadis et al. (2001). JAEG = Jaeger et al. (2001), the recommended rate. KUNZ = Kunz et al. (2002), the adopted rate. LUNA = Formicola et al. (2004), i.e., the LUNA (Laboratory for Underground Nuclear Astrophysics) collaboration. NACR = Angulo et al. (1999), NACRE. RATH = last version of the REACLIB provided by T. Rauscher and F. Thielemann, which is also available at <http://quasar.physik.unibas.ch/tommy>. RT = Rauscher & Thielemann (2000). OD94 = Oda et al. (1994). FFN8 = Fuller et al. (1982, 1985). LP00 = Langanke & Martínez Pinedo (2000). TAKA = Takahashi & Yokoi (1987). Table 1 is published in its entirety in the electronic edition of the *Astrophysical Journal*. A portion is shown here for guidance regarding its form and content.

equations is linearized and solved by means of a Raphson Newton technique. Let us also recall that, as in all our computations, the nuclear energy generation rate is always computed with the same, full, network adopted to describe the chemical evolution of the matter, without any kind of approximation. The network adopted in the present computations is the same as in Limongi & Chieffi (2003). We have assumed  $0.2 H_p$  of overshooting at the top of the convective core in central H burning. The nuclear cross sections have been updated with respect to those adopted in Limongi & Chieffi (2003) whenever possible. Table 1 shows the full reference matrix of all the processes taken into account in the network, together with its proper legend. Note that for the weak interaction rates,  $\beta^+$  and  $\beta^-$  mean the sum of both the electron capture and the  $\beta^+$  decay and the positron capture and the  $\beta^-$  decay, respectively. The dependence on the temperature of the weak interaction rates has been considered following Oda et al. (1994), Fuller et al. (1982), Langanke & Martínez-Pinedo (2000), and Takahashi & Yokoi (1987); see Table 1. The <sup>26</sup>Al requires a special treatment since the ground (Alg6 entry in Table 1) <sup>26</sup>Al<sup>g</sup> ( $J^\pi = 5^+$ ,  $\tau = 1.03 \times 10^6$  yr) and the isomeric states (Alm6 entry in Table 1) <sup>26</sup>Al<sup>m</sup> ( $J^\pi = 0^+$ ,  $\tau = 9.15$  s) do not come into statistical equilibrium for temperatures  $T \leq 10^9$  K (Ward & Fowler 1980; Gupta & Meyer 2001). For this reason we treat the ground and isomeric states of <sup>26</sup>Al as separate species for  $T \leq 10^9$  K, while we assume the two states to be in statistical equilibrium (and hence consider just one isotope) above this temperature. By the way, the Al26 entry in Table 1 refers to the total amount of <sup>26</sup>Al.

Mass loss has been included following the prescriptions of Vink et al. (2000, 2001) for the blue supergiant phase ( $T_{\text{eff}} > 12,000$  K), de Jager et al. (1988) for the red supergiant phase ( $T_{\text{eff}} < 12,000$  K), and Nugis & Lamers (2000) for the Wolf-Rayet phase. Additional models have been computed with the Langer (1989) mass-loss rate in the WNE+WCO phases.

The explosion of the mantle of the star is started by imparting instantaneously an initial velocity  $v_0$  to a mass coordinate of  $\sim 1 M_\odot$  of the presupernova model, i.e., well within the iron core. The propagation of the shock wave is computed by means of an explosive simulation code, developed by us, that solves the fully compressible reactive hydrodynamic equations using the piecewise parabolic method (PPM) of Colella & Woodward (1984) in the Lagrangean form, and  $v_0$  is properly tuned in order to

eject all the mass above the Fe core. The chemical evolution of the matter is computed by coupling the same nuclear network adopted in the hydrostatic calculations to the system of hydrodynamic equations. The nuclear energy generation is not taken into account in these simulations since we assume that it is always negligible with respect to both the kinetic and the internal energies. By taking advantage of the fact that the final yields mainly depend on the mass cut location (the mass coordinate that separates the ejecta from the compact remnant) and only mildly on the properties of the parameterized explosion, yields corresponding to different amounts of <sup>56</sup>Ni ejected can be easily obtained by fixing the mass cut by hand a posteriori (Limongi & Chieffi 2003). Here, for each star, we chose the mass cut in order to obtain  $0.1 M_\odot$  of <sup>56</sup>Ni ejected. By the way, let us note that since both <sup>26</sup>Al and <sup>60</sup>Fe are synthesized in quite external regions, their final yields do not depend on the particular choice of the mass cut since we assume in any case that at least a minimum amount of <sup>56</sup>Ni is ejected.

All these solar models has been computed by adopting an initial He abundance equal to 0.285 (by mass fraction), a global metallicity  $Z = 0.02$  (by mass fraction)—the relative abundances among the various nuclear species are taken from the Anders & Grevesse (1989) solar distribution. They range in mass between 11 and  $120 M_\odot$ , covering therefore the full range of masses that are expected to give rise to the Type II/Ib/Ic supernovae, as well as to the W-R populations. These models and the corresponding full set of yields are published and discussed below; for the moment we anticipate a few basic properties in Table 2. The following data are reported: the initial and final mass in solar masses (cols. [1] and [2]), the central H and He burning lifetimes in Myr (cols. [3] and [4]), the lifetime after the central He exhaustion in yr (col. [5]), the maximum sizes of the He and CO core masses in solar masses (cols. [6] and [7]), the bottom and top mass locations of the last C convective shell in solar masses (cols. [8] and [9], respectively), the central C mass fraction at the central He exhaustion (col. [10]), the total amount of time spent as O star (col. [11]) and W-R star (col. [12]) in yr and eventually the lifetimes as WNL (col. [13]), WNE (col. [14]), and WCO (col. [15]), all in years. We assume that the star enters the W-R phase when  $\log(T_{\text{eff}}) > 4$  and  $H_{\text{surf}} < 0.4$ , and we adopt the following usual definitions for the various W-R phases: WNL ( $10^{-5} < H_{\text{surf}} < 0.4$ ), WNE

TABLE 2  
BASIC EVOLUTIONARY PROPERTIES OF THE STELLAR MODELS

$M_{\text{ini}}$ ( $M_{\odot}$ ) (1)	$M_{\text{end}}$ ( $M_{\odot}$ ) (2)	$t_{\text{H}}$ (Myr) (3)	$t_{\text{He}}$ (Myr) (4)	$\Delta t_{\text{expl}}$ (yr) (5)	$M_{\text{He}}$ ( $M_{\odot}$ ) (6)	$M_{\text{CO}}$ ( $M_{\odot}$ ) (7)	$M_{\text{bottom}} (C_{\text{sh}})$ ( $M_{\odot}$ ) (8)	$M_{\text{top}} (C_{\text{sh}})$ ( $M_{\odot}$ ) (9)	$C_{\text{cen}}$ (mass fraction) (10)	$t_{\text{O}}$ (yr) (11)	$t_{\text{WR}}$ (yr) (12)	$t_{\text{WNL}}$ (yr) (13)	$t_{\text{WNE}}$ (yr) (17)	$t_{\text{WCO}}$ (yr) (15)
11.....	10.56	20.11	1.55	7.32E-4	3.473	1.749	1.5	1.739	0.359	0.00E+00	0.00E+00	0.00E+00	0.00E+00	0.00E+00
12.....	11.49	17.44	1.30	6.24E-4	3.912	1.971	1.6	1.916	0.361	0.00E+00	0.00E+00	0.00E+00	0.00E+00	0.00E+00
13.....	12.01	15.40	1.14	4.58E-4	4.363	2.212	1.8	2.011	0.350	0.00E+00	0.00E+00	0.00E+00	0.00E+00	0.00E+00
14.....	12.77	13.81	1.01	3.73E-4	4.816	2.461	1.7	2.322	0.341	2.07E+06	0.00E+00	0.00E+00	0.00E+00	0.00E+00
15.....	13.49	12.54	0.90	3.19E-4	5.293	2.720	1.8	2.574	0.344	5.66E+06	0.00E+00	0.00E+00	0.00E+00	0.00E+00
16.....	14.16	11.48	0.83	2.78E-4	5.765	2.989	2.0	2.734	0.347	6.69E+06	0.00E+00	0.00E+00	0.00E+00	0.00E+00
17.....	14.83	10.61	0.76	2.49E-4	6.209	3.253	2.0	3.151	0.344	7.34E+06	0.00E+00	0.00E+00	0.00E+00	0.00E+00
20.....	16.31	8.68	0.64	1.91E-4	7.643	4.354	1.8	4.354	0.321	7.08E+06	0.00E+00	0.00E+00	0.00E+00	0.00E+00
25.....	16.35	6.87	0.53	1.40E-4	10.223	6.148	2.2	6.148	0.287	6.02E+06	0.00E+00	0.00E+00	0.00E+00	0.00E+00
30.....	12.92	5.81	0.47	1.01E-4	12.680	8.011	1.9	7.154	0.263	5.19E+06	5.05E+04	5.05E+04	0.00E+00	0.00E+00
35.....	11.94	5.12	0.44	0.80E-4	14.687	8.508	2.3	8.203	0.251	4.62E+06	2.68E+05	1.16E+05	1.52E+05	0.00E+00
40.....	12.52	4.64	0.42	0.78E-4	16.493	8.983	2.5	8.600	0.247	4.16E+06	3.41E+05	1.10E+05	2.04E+05	2.64E+04
60.....	17.08	3.64	0.36	0.62E-4	25.172	12.623	3.7	11.623	0.218	3.18E+06	3.51E+05	6.18E+04	1.28E+05	1.61E+05
80.....	22.62	3.18	0.33	0.57E-4	34.706	17.408	5.0	16.332	0.187	2.66E+06	3.19E+05	4.43E+04	8.35E+04	1.91E+05
120.....	30.83	2.76	0.30	0.50E-4	48.553	24.519	7.8	22.790	0.156	2.19E+06	4.33E+05	1.78E+05	5.35E+04	2.02E+05
60t.....	19.93	3.93	0.34	0.64E-4	30.034	15.815	4.4	14.042	0.201	3.20E+06	3.36E+05	5.28E+04	1.02E+05	1.81E+05
120t.....	26.83	2.92	0.31	0.53E-4	44.400	21.360	6.6	19.601	0.170	2.58E+06	5.35E+05	2.48E+05	5.79E+04	2.28E+05

$[H_{\text{surf}} < 10^{-5}$  and  $(C/N)_{\text{surf}} < 0.1]$ , WNC  $[0.1 < (C/N)_{\text{surf}} < 10]$ , and WCO  $[(C/N)_{\text{surf}} > 10]$ . The main data concerning the  $^{26}\text{Al}$  and  $^{60}\text{Fe}$  yields are summarized in Table 3. The first column refers to the initial mass in solar masses. Columns (2)–(5) refer to the  $^{26}\text{Al}$  yield (all in solar masses): total (col. [2]), the wind contribution (col. [3]), the C and Ne shell contribution (col. [4]), and the explosive component (col. [5]). Columns (6)–(10) refer to the  $^{60}\text{Fe}$  yield (all in solar masses): total (col. [6]), the contributions of the radiative and convective He burning shell (cols. [7]–[9]), the convective C shell contribution (col. [10]), and the explosive component (col. [11]).

### 3. $^{26}\text{Al}$

$^{26}\text{Al}$  is an unstable nucleus (its terrestrial half-life is  $\tau_{1/2} \simeq 7.17 \times 10^5 \text{ y}$ ) produced almost exclusively by proton capture on  $^{25}\text{Mg}$ . Its synthesis occurs, in massive stars, essentially in three

different specific environments, i.e., the core H burning, the C and Ne convective shells, and the explosive Ne burning. Let us discuss each of these environments separately.

All over the mass range analyzed here,  $^{26}\text{Al}$  is produced in main sequence by the  $^{25}\text{Mg}(p, \gamma)^{26}\text{Al}$  reaction (hereafter MG25PG) and mainly destroyed by the  $\beta^+$  decay into  $^{26}\text{Mg}$  since the competing destruction process, i.e., the  $^{26}\text{Al}(p, \gamma)^{27}\text{Si}$  process, becomes efficient for  $T > 50 \times 10^6 \text{ K}$  and only our most massive model barely reaches such a temperature toward the end of the central H burning.

The conversion of the initial abundance of  $^{25}\text{Mg}$  into  $^{26}\text{Al}$  starts as soon as a star settles on the main sequence (since  $T_{\text{central}} \geq 30 \times 10^6 \text{ K}$ ) and comes to completion on a timescale of few million years, i.e., well within the central H burning lifetime. Figure 1 shows the temporal evolution of the  $^{26}\text{Al}$  mass fraction in the H convective core: a maximum is reached shortly after the beginning

TABLE 3  
 $^{26}\text{Al}$  AND  $^{60}\text{Fe}$  YIELDS

$M_{\text{ini}}$ ( $M_{\odot}$ ) (1)	$^{26}\text{Al}$ ( $M_{\odot}$ ) (2)	Wind ( $M_{\odot}$ ) (3)	Ne/C <sub>sh</sub> ( $M_{\odot}$ ) (4)	Explosive ( $M_{\odot}$ ) (5)	$^{60}\text{Fe}$ ( $M_{\odot}$ ) (6)	He <sub>sh</sub> ( $M_{\odot}$ ) (7)	He <sub>Schwarz</sub> ( $M_{\odot}$ ) (8)	He <sub>Ledoux</sub> ( $M_{\odot}$ ) (9)	C <sub>sh</sub> ( $M_{\odot}$ ) (10)	Explosive ( $M_{\odot}$ ) (11)
11.....	1.60E-5	1.16E-11	2.20E-6	1.38E-5	1.71E-6	3.0E-7	...	...	1.4E-6	1.0E-8
12.....	2.11E-5	2.91E-11	2.30E-6	1.71E-5	4.33E-6	2.0E-6	...	...	2.3E-6	...
13.....	2.45E-5	1.46E-10	2.50E-6	2.20E-5	7.56E-5	2.0E-6	...	...	...	7.4E-5
14.....	1.04E-4	4.37E-10	7.00E-5	3.40E-5	5.72E-6	1.8E-6	...	...	3.9E-6	...
15.....	1.32E-4	1.17E-09	8.00E-5	5.20E-5	6.28E-6	8.0E-7	...	...	5.4E-6	8.0E-8
16.....	6.80E-5	2.74E-09	1.00E-5	5.80E-5	4.39E-6	6.0E-7	...	...	6.0E-7	3.2E-6
17.....	6.87E-5	6.76E-09	1.50E-5	5.37E-5	7.96E-6	2.0E-7	...	...	4.0E-6	3.8E-6
20.....	5.43E-5	4.32E-08	1.80E-5	3.63E-5	1.56E-5	...	...	...	1.4E-5	1.6E-6
25.....	8.61E-5	3.93E-07	3.46E-5	5.11E-5	3.69E-5	...	...	...	3.2E-5	4.9E-6
30.....	9.93E-5	2.39E-06	2.61E-6	9.43E-5	1.49E-5	...	...	...	7.0E-6	7.9E-6
35.....	8.38E-5	1.14E-05	2.06E-5	5.18E-5	4.03E-5	...	...	...	3.3E-5	7.3E-6
40.....	1.21E-4	2.06E-05	3.44E-5	6.60E-5	6.23E-5	...	1.E-5	...	4.4E-5	8.3E-6
60.....	2.52E-4	6.94E-05	5.06E-5	1.32E-4	2.27E-4	...	1.E-4	6.0E-5	8.0E-5	4.7E-5
80.....	4.00E-4	1.32E-04	8.80E-5	1.80E-4	7.55E-4	...	6.E-4	1.4E-4	1.0E-4	5.5E-5
120.....	7.03E-4	2.82E-04	1.58E-4	2.63E-4	9.93E-4	...	8.E-4	2.5E-4	1.3E-4	6.3E-5
60t.....	2.97E-4	5.98E-05	5.02E-5	1.87E-4	5.50E-4	...	4.E-4	...	1.0E-4	5.0E-5
120t.....	6.97E-4	3.50E-04	1.10E-4	2.37E-4	8.60E-4	...	7.E-4	...	1.0E-4	6.0E-5

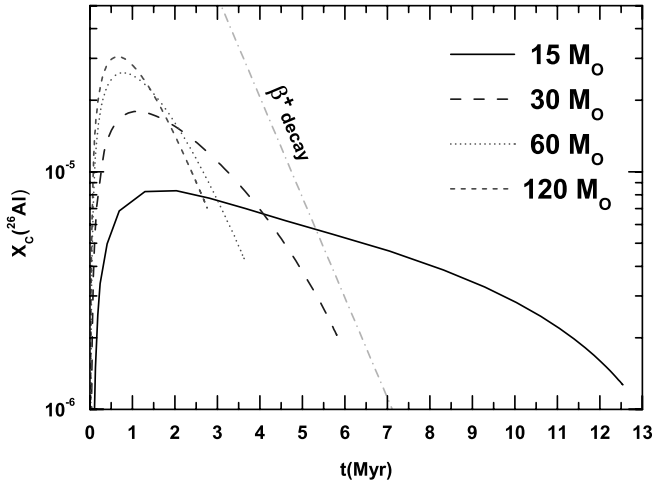


FIG. 1.—Temporal evolution of the central  $^{26}\text{Al}$  mass fraction during core H burning. The solid, long-dashed, dotted, and short-dashed lines refer to the 15, 30, 60, and  $120 M_{\odot}$  models, respectively. The dot-dashed line refers to a pure  $^{26}\text{Al}$  decay. [See the electronic edition of the Journal for a color version of this figure.]

of the central H burning, followed by a progressive decrease mainly due to the  $\beta^+$  decay. Since  $^{26}\text{Al}$  continues to be produced also after the maximum, its decline is shallower than that of a pure decay (Fig. 1, dot-dashed line). By the way, it is such a prolonged production that preserves some  $^{26}\text{Al}$  in the H convective core up to the end of the central H burning. In fact, if the slope of the decline would follow a pure decay after the maximum, essentially all the  $^{26}\text{Al}$  would decay by the time the star exhausts the H in the center. The solid, long-dashed, dotted, and short-dashed lines refer to the 15, 30, 60, and  $120 M_{\odot}$ , respectively.

Since the efficiency of the MG25PG reaction rate scales directly with the initial mass, the larger the initial mass the higher the maximum  $^{26}\text{Al}$  mass fraction abundance, the faster the  $^{25}\text{Mg}$  consumption and hence the faster the  $^{26}\text{Al}$  decline. Hence, if the efficiency of the MG25PG were the only parameter to control the scaling of the  $^{26}\text{Al}$  mass fraction abundance at the central H exhaustion with the initial mass of the star, one should obtain an inverse scaling of the central  $^{26}\text{Al}$  mass fraction at the central H exhaustion with the mass. However, the models show a strong direct scaling. Such a result is the obvious consequence of the strong shortening of the central H-burning lifetime with the initial mass that freezes the central  $^{26}\text{Al}$  abundance progressively at earlier times (and hence at higher abundances). Of course, a direct scaling between the  $^{26}\text{Al}$  mass fraction and the initial mass of a star does not imply, by itself, a direct scaling between the total amount of  $^{26}\text{Al}$  (in solar masses) produced by the H burning and the initial mass. In fact, it is the size of the convective core that really determines how much  $^{26}\text{Al}$  is produced in total, and since it scales directly with the initial mass, the direct scaling between  $^{26}\text{Al}$  produced and initial mass is secured.

At central H exhaustion, the  $^{26}\text{Al}$  is located both in the He core and in the region of variable H left behind by the receding convective core. Since the He burning easily and quickly destroys the  $^{26}\text{Al}$  [via the  $(n, \alpha)$  and  $(n, p)$  reactions—the neutrons being released by the  $^{13}\text{C}(\alpha, n)^{16}\text{O}$  process] the amount of  $^{26}\text{Al}$  synthesized by central H burning and really preserved up to the explosion is just the one located in the H-rich layers plus the one locked in the fraction of the He core that will not be affected by the He burning. If the dredge-up and the mass loss were not effective, this  $^{26}\text{Al}$  would be ejected altogether by the explosion, while the occurrence of these two phenomena may anticipate such an ejection

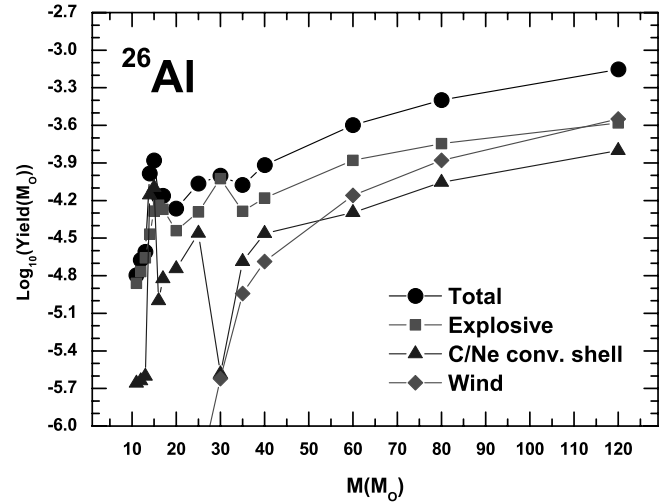


FIG. 2.— $^{26}\text{Al}$  yields as a function of the initial mass. [See the electronic edition of the Journal for a color version of this figure.]

at earlier times and also increase the amount of  $^{26}\text{Al}$  ejected into the interstellar medium. In our models three mass intervals may be identified: (1) Stars between 11 and  $30 M_{\odot}$  undergo a dredge-up episode that does not enter into the He core, and the mass loss is weak enough that all these stars end their life with an H-rich envelope; since the He convective shell extends almost up to the base of the H burning shell, only the tiny amount of  $^{26}\text{Al}$  present in the region of variable H left by the receding H convective core and engulfed in the convective envelope is ejected in the interstellar medium. (2) Stars between 35 and  $40 M_{\odot}$  experience a dredge-up episode that does not enter the He core as well, but the mass loss is strong enough that a fraction of the He core is also ejected outward; since the mass loss erodes the He core before the formation of the He convective shell, the  $^{26}\text{Al}$  present in these layers is preserved by the destruction and goes to increase the amount of  $^{26}\text{Al}$  ejected in the interstellar medium. (3) Stars more massive than  $40 M_{\odot}$  do not show any dredge-up episode, and the mass loss is so strong that a substantial fraction of the He core is ejected through the stellar wind; as a consequence, a larger amount of  $^{26}\text{Al}$  present in the He core is preserved from the destruction and ejected. As for the first two mass intervals, the wind starts expelling  $^{26}\text{Al}$  as soon as the star becomes a red (super)giant. On the other hand, stars in the upper mass interval begin to eject  $^{26}\text{Al}$  only when the total mass of the star reduces enough that layers processed by the H burning are exposed to the surface (i.e., when the star becomes a W-R). Let us eventually note that only a very tiny fraction of the original  $^{25}\text{Mg}$  is ejected in the interstellar medium as  $^{26}\text{Al}$  (mainly because of the substantial  $^{26}\text{Al}$  decay during the core H burning), and also that this  $^{26}\text{Al}$  is of semisecondary origin since only the  $^{25}\text{Mg}$  depends on the initial metallicity  $Z$  and obviously not the protons (the true secondary nuclei are the ones formed by reactions in which both the target and the projectile depend on the initial metallicity, for example, as in the  $s$ -process production). Figure 2 shows, as diamonds, the amount of  $^{26}\text{Al}$  expelled through the stellar wind as a function of the initial mass; the observed trend is the obvious consequence of what has been discussed above, i.e., it is the result of the direct scaling of (1) the size of the H convective core, (2) the  $^{26}\text{Al}$  mass fraction left by the central H burning, and (3) the mass loss efficiency with the initial mass.

Once the star moves beyond the central H burning, the “habitat” becomes very hostile to the survival of  $^{26}\text{Al}$ . First of all, how already mentioned above, the He burning simply destroys

$^{26}\text{Al}$  through neutron captures. Second, the half-life of  $^{26}\text{Al}$  has a tremendous dependence on the temperature: it reduces to  $\sim 0.19$  yr already at  $\log T = 8.4$ , to  $\sim 13$  hr at  $\log(T) = 8.6$ , and to  $13/2$  m in the range  $9 < \log(T) < 9.6$ . Third, efficient photodisintegration quickly destroys  $^{26}\text{Al}$  when the temperature raises above, say,  $\log(T) = 9.3$ . Such a temperature limit obviously constrains a possible  $^{26}\text{Al}$  production to the C- and/or Ne-burning shells.

As for the C shell, its typical temperature [ $\log(T) < 9.08$ ] does not allow in general a substantial production of  $^{26}\text{Al}$ . However, after the central Si burning, the strong contraction (and heating) of the inner core that precedes the final gravitational collapse, induces a strong temperature increase of the C-burning shell [up to, roughly,  $\log(T) \sim 9.255$ ]. If, at this stage, such a burning occurs in an efficient convective shell, a substantial amount of  $^{26}\text{Al}$  is produced. Let us discuss this production in a more detailed way. The processes that produce and destroy  $^{26}\text{Al}$  in these conditions are once again the MG25PG and the beta decay. The MG25PG reaction rate depends on the MG25PG cross section but also on the abundances of  $^{25}\text{Mg}$  and protons. The  $^{25}\text{Mg}$  that now enters in the  $^{26}\text{Al}$  production comes directly from the initial CNO abundance, via the sequence  $(\text{CNO})_{\text{ini}} \rightarrow {}^{14}\text{N} \rightarrow {}^{22}\text{Ne} \rightarrow {}^{25}\text{Mg}$ , while the protons are mainly produced by the  ${}^{12}\text{C}({}^{12}\text{C}, p){}^{23}\text{Na}$  and the  ${}^{23}\text{Na}(\alpha, p){}^{26}\text{Mg}$  processes. By the way, note that the main proton poison is not the  $^{25}\text{Mg}$  but, instead, the  ${}^{23}\text{Na}$  through the  $(p, \alpha)$  channel. The high temperature influences the  $^{26}\text{Al}$  production both because it raises the MG25PG cross section and because it strongly increases the proton density by increasing the cross sections of both the processes that provide the bulk of protons. On the other hand, the presence of a convective environment is also crucial because it continuously brings fresh  ${}^{12}\text{C}$  and  $^{25}\text{Mg}$ , where the  $^{26}\text{Al}$  production occurs and simultaneously brings the freshly made  $^{26}\text{Al}$  to much lower temperatures where its lifetime increases enormously.

At variance with the C burning,  $^{26}\text{Al}$  is always produced by the Ne burning (both in the center and in the shell). A substantial amount of  $^{25}\text{Mg}$  is left unburned by the C burning, and the protons needed to activate the  ${}^{25}\text{Mg}(p, \gamma){}^{26}\text{Al}$  reaction mainly come from the  ${}^{23}\text{Na}(\alpha, p){}^{26}\text{Mg}$  reaction ( ${}^{23}\text{Na}$  being one of the products of C burning), the values of  $\alpha$ -particles being provided by the  ${}^{20}\text{Ne}(\gamma, \alpha){}^{16}\text{O}$  photodisintegration. Again, the most effective protons poison is the  ${}^{23}\text{Na}(p, \alpha){}^{20}\text{Ne}$ . In a radiative environment the  $^{26}\text{Al}$  “equilibrium” abundance depends on the local balance between production and destruction so that, as soon as the  ${}^{20}\text{Ne}$  photodisintegration weakens for lack of fuel, the abundance of the values of  $\alpha$ -particles drop as well, and the proton production channels dry up: no more  $^{26}\text{Al}$  can be produced, and its short lifetime at these high temperatures leads quickly to its total destruction. Once again only the presence of an efficient convective shell could act as a preservation buffer. Since most of the stars do not reach the onset of the explosion with an efficient Ne convective shell, in general only the small equilibrium abundance of  $^{26}\text{Al}$  located within the radiative Ne burning shell is present at the beginning of the core collapse. There are two exceptions: the 14 and the 15  $M_{\odot}$  models. Stars within this mass interval are characterized by the lack of a C convective shell, at the end of the central Si burning, and by the formation of a Ne convective shell very close to the region where it was previously efficient a carbon convective shell. During the last strong contraction of the core that precedes the final collapse, such a Ne convective shell penetrates the C-rich region with the consequence of producing a huge amount of  $^{26}\text{Al}$ .

The  $^{26}\text{Al}$  synthesized in the C (or Ne/C) convective shell is located close enough to the iron core that is partially destroyed by the passage of the shock wave. In general, the larger the mass,

the larger the amount of  $^{26}\text{Al}$  that survives the explosion (Table 3). The blue triangles in Figure 2 show the  $^{26}\text{Al}$  yield produced in this convective shell that survived to the explosion as a function of the initial mass. The general increase of this yield with the mass depends on the fact that both the mass size and the peak temperature of the C (or Ne/C) convective shell scale directly with the mass. The peak around the 15  $M_{\odot}$  model, as already discussed above, is due to the presence of an extended Ne convective shell that engulfs part of the C-rich region. The minimum yield around the 30  $M_{\odot}$  is the natural consequence of the lack of an active C (and Ne) convective shell at the moment of the explosion. The  $^{26}\text{Al}$  produced by the C and/or Ne shell is of semisecondary origin (as the one produced by the H burning) because the  $^{25}\text{Mg}$  is secondary while protons are primary.

$^{26}\text{Al}$  is also produced during the explosion at a typical temperature of the order of  $\sim 2.3$  billion degrees. Such a condition occurs within the C convective shell and the main process that controls its production is once again the MG25PG process while its destruction is now controlled, roughly paritetically, by the  $(n, p)$  and  $(n, \alpha)$  processes. The  $^{25}\text{Mg}$  now comes mainly from the  $(n, \gamma)$  capture on  ${}^{24}\text{Mg}$ , this isotope being a primary outcome of the C and Ne burning. The neutron density that enters in both the production and destruction of  $^{26}\text{Al}$  is determined by the competition among several processes: the main neutron producers are  $(\alpha, n)$  captures on  ${}^{26}\text{Mg}$ ,  ${}^{25}\text{Mg}$ ,  ${}^{21}\text{Ne}$ , and  ${}^{29}\text{Si}$ , plus the  $(p, n)$  capture on  ${}^{28}\text{Al}$ , while the main neutron poisons are the  $(n, \gamma)$  captures on  ${}^{24}\text{Mg}$ ,  ${}^{16}\text{O}$  and  ${}^{20}\text{Ne}$ . The proton density that enters the MG25PG rate is mainly determined by the competition between the production that occurs via the  $(\alpha, p)$  captures on  ${}^{20}\text{Ne}$ ,  ${}^{24}\text{Mg}$ ,  ${}^{27}\text{Al}$ , and  ${}^{23}\text{Na}$  and the destruction that occurs via the  $(p, \gamma)$  capture on  ${}^{26}\text{Mg}$ ,  ${}^{20}\text{Ne}$ ,  ${}^{24}\text{Mg}$ ,  ${}^{27}\text{Al}$ ,  ${}^{25}\text{Mg}$ , and  ${}^{30}\text{Si}$ , plus the  $(p, n)$  reaction on  ${}^{28}\text{Al}$ . Figure 2 shows the contribution of the explosive burning to the synthesis of  $^{26}\text{Al}$  as filled red squares. To understand the trend of the explosive yield with the mass it is necessary to recall that the final mass-radius (MR) relation at the moment of the core collapse plays a fundamental role for the synthesis of many nuclei, because it mainly determines the amount of matter exposed to the various explosive burnings (Chieffi et al. 2000; Chieffi & Limongi 2002). Such a relation strongly depends on the behavior of the C, Ne, and O shell burnings all along the evolution of a star. The general rule is that the stronger is a shell burning, the slower is the contraction and hence the shallower is the final MR relation; it is also worth recalling that a stronger shell burning usually implies a wider (in mass) convective shell. Figure 3 shows the final MR relation for a subset of stars in the present grid. By the way, since the blast wave is essentially radiation-dominated, the spatial location where the peak temperature drops to, say, 2.3 billion degrees occurs around  $0.01 - 0.02 R_{\odot}$ , the exact value depending (quite mildly) on the explosion energy. The figure clearly shows that there is a nonmonotonic dependence on the initial mass: although a general trend exists, in the sense that the larger the mass the steeper this relation, two inversions exist: the first one between 17 and 20  $M_{\odot}$  and the second one between 30 and 35  $M_{\odot}$ . The first inversion marks the first mass (20  $M_{\odot}$ ) forming a very extended last C convective shell that slows down the gravitational contraction of the core and hence halts the direct scaling between the compactness of the inner layers and the initial mass. The second inversion, occurring around the 35  $M_{\odot}$  model, marks the minimum mass that forms a single well-settled C convective shell that lasts up to the explosion. Also, in this case the formation of a single very active C convective shell counterbalances the increase in the gravitational contraction induced by the increase of the total mass. The explosive yields shown in Figure 2 follow

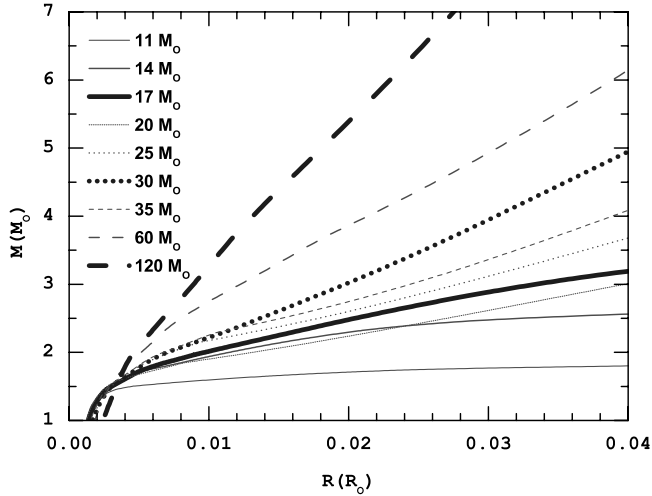


FIG. 3.—Final MR relation at the beginning of the core collapse for a subset of the grid models. [See the electronic edition of the *Journal* for a color version of this figure.]

almost exactly the general trend shown by the MR relation: there is a general direct scaling between the explosive  $^{26}\text{Al}$  and the initial mass, but with two minima corresponding to the two masses quoted above.

The circles in Figure 2 show the total yield of  $^{26}\text{Al}$  as a function of the initial mass. It is quite evident that for the largest majority of the stars in the present mass range  $11 < M/M_\odot < 120$  the explosive component is the major contributor to the total yield. Only around  $15 M_\odot$  the  $^{26}\text{Al}$  produced in the advanced hydrostatic burnings dominate the final yield. The wind component to the total is always negligible up to a mass of, say,  $60 M_\odot$ . Above this mass, it contributes roughly 30% of the global outcome. Note, however, that although the explosive burning is the overall major producer of  $^{26}\text{Al}$  within the full initial mass interval analyzed here, the  $^{26}\text{Al}$  produced by both the H burning and the C/Ne shell cannot be ignored in the computation of the final budget of  $^{26}\text{Al}$  produced by a generation of massive stars.

There are many quite uncertain basic stellar parameters that may significantly alter the final  $^{26}\text{Al}$  yields shown in Figure 2. We have explored a few of them:

1. The adopted initial  $^{25}\text{Mg}$  abundance (usually scaled solar) constitutes the main buffer from which the  $^{26}\text{Al}$  is produced in the main sequence and a change of its initial (assumed) abundance reflects linearly on the final amount of  $^{26}\text{Al}$  ejected by the wind. In other words, a doubling of the initial  $^{25}\text{Mg}$  leads to a doubling of the  $^{26}\text{Al}$  ejected through the wind.

2. The size of the H convective core certainly plays a pivotal role since it affects both directly and indirectly the final  $^{26}\text{Al}$  yield. The direct influence occurs in the main sequence because it contributes to determine its abundance, by mass fraction, as well as its distribution within the star at the end of the core H burning; the indirect influence occurs through its major role in determining the He core mass, which is the main parameter driving all the further evolution of a star. In order to study the dependence of the  $^{26}\text{Al}$  yield on the size of the H convective core, we recomputed the full presupernova evolution plus the explosive burning of a  $60 M_\odot$  and a  $120 M_\odot$  by adopting  $0.5 H_p$  of overshooting (instead of the basic  $0.2 H_p$ ) in core H burning. The main results are shown in the last two rows of Table 2 and Table 3. The first thing worth noting is that the increase of the size of the H convective core has two opposite effects on the two masses: the

total  $^{26}\text{Al}$  yield increases by 18% in the  $60 M_\odot$ , while it remains roughly constant in the  $120 M_\odot$ . A closer look to the various components shows that the wind component reduces by 16% in the  $60 M_\odot$  while it increases by 24% in the  $120 M_\odot$ . The sum of the other two components shows, on the other hand, the opposite trend, i.e., it increases in the smaller mass and reduces in the larger one. Such results are the consequence of a complex interplay among several phenomena. First of all an increase of the convective core has two opposite effects: it increases the region where the initial  $^{25}\text{Mg}$  is converted in  $^{26}\text{Al}$ , but it also leads to a lower  $^{26}\text{Al}$  abundance by mass fraction at the core H exhaustion (because the H-burning lifetime increases). The final balance between these two opposite phenomena is not predictable a priori, but it happens that the first effect prevails on the second one so that at last more  $^{26}\text{Al}$  (in solar masses) is produced overall. However, such an occurrence is not sufficient to determine how the  $^{26}\text{Al}$  wind component depends on the size of the convective core, because another crucial role is played by mass loss: a change of the size of the convective core strongly affects the path followed by a star in the HR diagram and hence the total amount of mass that it loses. In the  $60 M_\odot$  case, the standard and test models lose similar amounts of mass in the main sequence; however, while the standard model spends a consistent fraction of the central He burning phase as a red supergiant, where it loses a very large amount of mass, the model with the larger convective core moves much earlier to the blue, where the average mass-loss rates are significantly lower. The final result is that the test model loses less mass, reaching the final collapse with a total mass of  $19.93 M_\odot$ , i.e.,  $2.8 M_\odot$  more than the standard case. This explains why the test  $60 M_\odot$  ejects less  $^{26}\text{Al}$  through the wind than its standard counterpart. In the  $120 M_\odot$  case the opposite happens: the test model loses much more mass than the standard model: in fact its final mass is  $26.83 M_\odot$ , i.e.,  $4 M_\odot$  less than the standard model. In this specific case the luminosity increase in central H burning (due to the increase of the convective core) allows the model to enter (for a consistent amount of time) a region of the HR diagram where mass loss is very efficient (see Vink et al. 2000, 2001). This explains why the amount of  $^{26}\text{Al}$  present in the wind is larger in the test than in the standard model. As for the  $^{26}\text{Al}$  produced by the advanced (C/Ne) burnings plus the explosion, we found that these components scale directly with the size of the convective core in the  $60 M_\odot$  and inversely in the  $120 M_\odot$ . The reason is simply that the amount of  $^{26}\text{Al}$  produced both in the advanced and in the Ne explosive burnings scale directly with the size of the He core mass, and Table 2 shows that this parameter increases with the size of the convective core in the  $60 M_\odot$ , while it decreases in the  $120 M_\odot$  case: this last (apparently) unexpected result is due to the strong increase of the mass-loss rate in the  $120 M_\odot$  stellar model computed with  $0.5 H_p$  of overshooting.

3. We have also explored the influence of the MG25PG cross section on the  $^{26}\text{Al}$  produced by the H burning and expelled through the wind. Although the uncertainty quoted for this process (e.g., Iliadis et al. 2001) is of the order of a factor of 2 in the temperature range  $0.02 \leq T_9 \leq 0.2$ , we preferred to explore the general theoretical dependence of the  $^{26}\text{Al}$  (ejected by the wind) on the MG25PG cross section in a range of values wider than (currently) expected. Hence, we have performed a few tests on both the  $60$  and the  $120 M_\odot$  by multiplying and dividing this cross section by factors of 3 and 10. Table 4 shows the results of these tests in the first four rows: the first column shows the cross section adopted in the test while the fourth and fifth columns show the amount of  $^{26}\text{Al}$  (in solar masses) present in the wind for the  $60$  and  $120 M_\odot$  star models, respectively. These tests show that

TABLE 4  
TESTS ON THE  $^{26}\text{Al}$  YIELDS

Test (1)	Component (2)	25 $M_{\odot}$ (3)	60 $M_{\odot}$ (4)	120 $M_{\odot}$ (5)
$^{25}\text{Mg}$ (initial) $\times 2$ .....	Wind	...	1.34(−4)	5.64(−4)
$^{25}\text{Mg}(p, \gamma)^{26}\text{Al} \times 10$ .....	Wind	...	4.16(−5)	2.20(−4)
$^{25}\text{Mg}(p, \gamma)^{26}\text{Al} \times 3$ .....	Wind	...	4.60(−5)	2.33(−4)
$^{25}\text{Mg}(p, \gamma)^{26}\text{Al} \times 0.33$ .....	Wind	...	1.09(−4)	3.32(−4)
$^{25}\text{Mg}(p, \gamma)^{26}\text{Al} \times 0.1$ .....	Wind	...	7.79(−5)	2.10(−4)
0.5 $H_p$ overshooting in $H_{\text{burning}}$ .....	Wind	...	5.98(−5)	3.50(−4)
0.5 $H_p$ overshooting in $H_{\text{burning}}$ .....	Total	...	2.97(−4)	6.97(−4)
$^{26}\text{Al}(n, p)^{26}\text{Mg} \times 2$ & .....	...	...	...	...
$^{26}\text{Al}(n, \alpha)^{23}\text{Na} \times 2$ .....	Explosive	3.13(−5)	7.80(−5)	...
$^{24}\text{Mg}(n, \gamma)^{25}\text{Mg} \times 2$ .....	Explosive	8.00(−5)	2.11(−4)	...
$^{25}\text{Mg}(p, \gamma)^{26}\text{Al} \times 2$ .....	Explosive	8.20(−5)	2.09(−4)	...

(a) the amount of  $^{26}\text{Al}$  ejected by the wind does not scale monotonically with the efficiency of this cross section but, instead, that it first increases as the cross section decreases and then begins to decrease when the cross section drops below  $\frac{1}{3}$  of the reference one, and (b) the amount of  $^{26}\text{Al}$  ejected by the wind depends only mildly on a systematic variation of the cross section, since it varies by less than a factor of 2 over a huge variation of the MG25PG cross section. To understand these results it is necessary to analyze in more detail the synthesis of  $^{26}\text{Al}$  in H burning. In the following we discuss the behavior of the 60  $M_{\odot}$ , but the same analysis holds over the full mass range analyzed here. Figure 4 shows the variation of the abundance of the  $^{26}\text{Al}$  in the convective core as a function of time for the five values of the cross section: the thin dotted line refers to the case in which the enhancement factor (EF) of the standard cross section is 10, the long-dashed one to an EF = 3, the black solid line to the standard case, the short-dashed line to an EF =  $\frac{1}{3}$ , and the short-dashed line to an EF = 0.1. The test with the highest EF simulates the extreme case in which the  $^{25}\text{Mg}$  is completely converted in  $^{26}\text{Al}$  just at the beginning of the H burning. In this case the maximum  $^{26}\text{Al}$  abundance is the highest, but the following decline is also the steepest (it practically follows a pure decay) because no more  $^{25}\text{Mg}$  is left to feed the  $^{26}\text{Al}$  abundance at late times. As the EF reduces, the maximum equilibrium

abundance of the  $^{26}\text{Al}$  drops accordingly, while the final  $^{26}\text{Al}$  abundance progressively increases due to the larger availability of  $^{25}\text{Mg}$  at late time. This trend, however, naturally comes to an end when the cross section becomes so slow that the timescale over which  $^{25}\text{Mg}$  converts into  $^{26}\text{Al}$  becomes longer than the H burning timescale. At this point the final abundance of  $^{26}\text{Al}$  is mainly controlled by the total amount of  $^{25}\text{Mg}$  destroyed: the lower the rate, the smaller the amount of  $^{25}\text{Mg}$  converted in  $^{26}\text{Al}$  and hence the smaller its final abundance. A cross section 10 times lower than our standard case is low enough to enter such a regime. By the way, it goes without saying that the physical evolution of the star does not depend at all on the rate of this process, so that all the timescales, the amount of mass lost, the penetration of the dredge-up and so on remain rigorously identical in all these tests.

4. Since most of the  $^{26}\text{Al}$  ejected in the interstellar medium is anyway synthesized by the passage of the shock wave, we have also explored its sensitivity to the rates of the processes involved in its production in Ne explosive burning. Of course, the number of factors that can influence the explosive production of  $^{26}\text{Al}$  is very large and includes all the factors that may affect the final mass-radius relation [as, e.g., the  $^{12}\text{C}(\alpha, \gamma)^{16}\text{O}$ ]; such a deep analysis goes well beyond the purposes of this paper. We have explored the influence of a few rates, namely, the two main processes involved in the synthesis of  $^{26}\text{Al}$ , i.e., the  $^{24}\text{Mg}(n, \gamma)^{25}\text{Mg}$  and the  $^{25}\text{Mg}(p, \gamma)^{26}\text{Al}$ , as well as the two processes that control its destruction, i.e., the  $^{26}\text{Al}(n, p)^{26}\text{Mg}$  and the  $^{26}\text{Al}(n, \alpha)^{23}\text{Na}$ . In particular, we have recomputed three explosions for the two masses 25 and 60  $M_{\odot}$ , the first one doubling the cross sections of both the neutron captures on  $^{26}\text{Al}$ , the second one doubling the  $n$  capture on  $^{24}\text{Mg}$ , and the last one by doubling the MG25PG. The results are shown in the eighth to eleventh rows in Table 4. Since the efficiency of any process depends on its rate (i.e., the cross section times the abundances of the involved nuclei) rather than just on its cross section, the tests shown in Table 4 may also be reinterpreted as due to a change by a factor of 2 of any of the two nuclear species involved in the given process. This means that the tests concerning, in particular, the influence of the  $^{24}\text{Mg}(n, \gamma)^{25}\text{Mg}$ , the  $^{26}\text{Al}(n, p)^{26}\text{Mg}$ , and the  $^{26}\text{Al}(n, \alpha)^{23}\text{Na}$  on the explosive synthesis of the  $^{26}\text{Al}$  may also be seen as tests in which the neutron density has been increased by a factor of 2. Since a doubling of the  $^{24}\text{Mg}(n, \gamma)^{25}\text{Mg}$  rate increase the explosive  $^{26}\text{Al}$  by roughly 60% while the simultaneous doubling of both the  $^{26}\text{Al}(n, p)^{26}\text{Mg}$  and the  $^{26}\text{Al}(n, \alpha)^{23}\text{Na}$  rates reduces the  $^{26}\text{Al}$  by roughly 40%, it is clear that the two effects almost cancel out, so that we feel confident in concluding that a changing of the

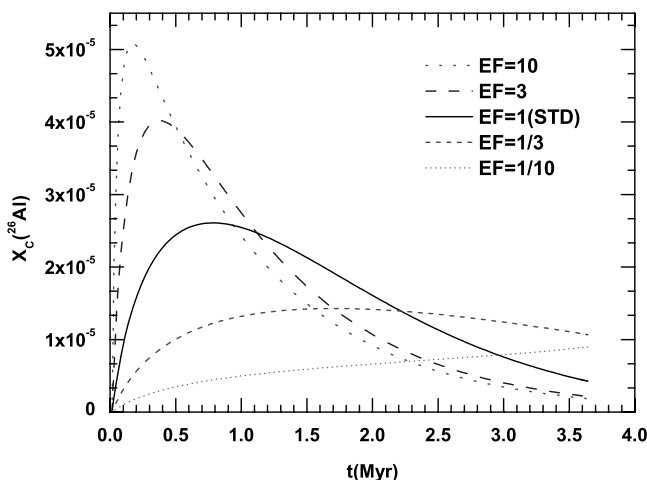


FIG. 4.—Temporal variation of the central  $^{26}\text{Al}$  mass fraction during core H burning in a 60  $M_{\odot}$ . The black solid line refers to the standard evolution, while the other four lines show the cases in which the cross section of the  $^{25}\text{Mg}(p, \gamma)^{26}\text{Al}$  reaction is multiplied by an EF. [See the electronic edition of the Journal for a color version of this figure.]



neutron density plays a minor role on the explosive synthesis of the  $^{26}\text{Al}$ . Let us stress here, as a general warning, that the neutron and proton equilibrium abundances that enter in the various processes depend on the balance among a variety of similarly efficient processes, so that all of them should be carefully checked in order to understand whether these equilibrium abundances are reliable or not.

Let us finally explicitly mention other important sources of uncertainty that could affect the  $^{26}\text{Al}$  yield:

1. The C abundance left by the He burning provides the main fuel that feeds both the C and the Ne burning (whose abundance derives directly from the C one) and hence it regulates the birth and the development of all the convective shells and hence, in turn, the final MR relation. Unfortunately, as is well known, this value is not firmly established because it depends on the still very uncertain cross section of the  $^{12}\text{C}(\alpha, \gamma)^{16}\text{O}$  process together with the adopted mixing scheme in central He burning.

2. We have shown how critical the presence of a convective shell and the efficiency of mixing are to preserving the  $^{26}\text{Al}$  produced in the C (Ne/C) burning shell; any change in their mass size and/or in the efficiency of mixing could significantly alter their contribution to the total yield (see also Weaver & Woosley 1993).

It goes without saying that only the computation of a series of evolutionary tracks may really provide a quantitative estimate of these additional important uncertainties.

Before closing this section let us compare our final yields with the other ones available in the literature. We already published yields for  $^{26}\text{Al}$  in 2003 and 2004 (Limongi & Chieffi 2003; Chieffi & Limongi 2004); those yields (the  $^{26}\text{Al}$  ones only), unfortunately, must be totally disregarded, since when we updated the full set of cross sections adopted in the evolutionary code, we found that the  $^{26}\text{Al}(p, \gamma)^{27}\text{Si}$  cross section present in the REACLIB database, and based on the Caughlan & Fowler (1988) formula, was wrong. Figure 5 shows the  $^{26}\text{Al}$  yields by WW95 (*filled squares*), Rauscher et al. (2002) (*filled triangles*), Thielemann et al. (1996) (*filled rhombs*), Meynet et al. (1997) (*open circles*), Palacios et al. (2005) (*open squares*) and Langer et al. (1995) (*open rhombs*) together with the present ones (marked as “this paper”; *filled circles*). The first thing worth noting is that our set of models is the only one that fully extends over the full range of the massive stars. As we have already said above, for historical reasons two parallel fields of research may be identified: the first one (mainly involving Woosley and coauthors), addressed the full evolution of stellar models (including the computation of the passage of the shock wave) but did not extend the explored mass interval above 35–40  $M_{\odot}$ , and the second one (which includes mainly European groups) involved the study of the central H and He burning phases in a wide mass interval (up to 120  $M_{\odot}$ ) by including the mass loss and hence fully exploring the properties of the W-R stars. The WW95  $^{26}\text{Al}$  yields show remarkable similarities with ours: both sets of yields show two maxima, a first one around 15–20  $M_{\odot}$  and a second one around 30–35  $M_{\odot}$ , the WW95 ones being slightly shifted toward more massive stars. We already discussed above how these two peaks are related to the temporal evolution of the C convective shell, and hence these strong similarities clearly point toward a quite similar presupernova evolution. The quite larger WW95 yields between 25 and 40  $M_{\odot}$  are probably at least partially due to the contribution of the  $\nu$  process that we neglect. WW95 quote the  $^{26}\text{Al}$  yield for the 25  $M_{\odot}$  without the  $\nu$  contribution and the value closely matches our yield. The Rauscher et al. (2002) yields are

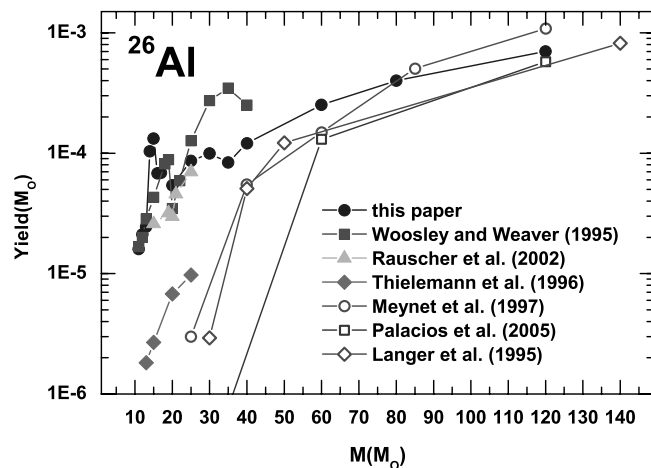


FIG. 5.— Comparison among the  $^{26}\text{Al}$  yields provided by various authors. [See the electronic edition of the Journal for a color version of this figure.]

an upgrade of the WW95 for the solar metallicity; note that they do not show any more a strong peak around a 20  $M_{\odot}$ , which means that something in the properties of the C convective shell has changed with respect to the older WW95 stellar models. Anyway, we feel confident to say that these three sets of yields lead to quite similar predictions. An additional set of yields for this mass interval was provided by Thielemann et al. (1996): these yields are much lower than all the other ones probably because they come from the evolution of just pure He cores computed by adopting a quite poor network in the hydrostatic burnings. Historically, stars more massive than, say, 35  $M_{\odot}$  have been studied almost exclusively up to the end of the central He burning, so that only the  $^{26}\text{Al}$  present in the wind has been (widely) discussed in the literature. The latest  $^{26}\text{Al}$  yields in this mass interval are those provided by Langer et al. (1995), Meynet et al. (1997), and Palacios et al. (2005). Note that, for homogeneity reasons, only the nonrotating models are shown. Figure 5 shows that the differences among these theoretical yields are confined within a factor of 2.

#### 4. $^{60}\text{Fe}$

$^{60}\text{Fe}$  is an unstable nucleus (its terrestrial half-life is  $\tau_{1/2} \simeq 1.5 \times 10^6 \text{ y}$ ) that lies slightly out of the stability valley, its closest stable neighbor being  $^{58}\text{Fe}$ . It is mainly produced by neutron capture on the unstable nucleus  $^{59}\text{Fe}$  and destroyed by the  $(n, \gamma)$  process. Since its closest parent,  $^{59}\text{Fe}$ , is unstable, the  $^{59}\text{Fe}(n, \gamma)$  process must compete with the  $^{59}\text{Fe}(\beta^-)$  decay to produce an appreciable amount of  $^{60}\text{Fe}$ . An order-of-magnitude estimate of the neutron densities needed to cross the  $^{59}\text{Fe}$  bottleneck may be derived by equating the  $(n, \gamma)$  and  $\beta^-$  decay rates: a value of the order of  $3 \times 10^{10} \text{ n cm}^{-3}$  is obtained at temperatures lower than  $\log(T) = 8.7$ . Above this temperature the half-life of  $^{59}\text{Fe}$  (whose terrestrial value is  $\simeq 44$  days) reduces systematically, dropping to  $\sim 6$  days at  $\log(T) = 9.0$  and to  $\sim 1$  hr at  $\log(T) = 9.6$ , while the  $^{59}\text{Fe}(n, \gamma)$  cross section varies very mildly with the temperature. As a consequence, the neutron density needed to cross the  $^{59}\text{Fe}$  bottleneck steeply increases with the temperature: it raises to  $\simeq 3 \times 10^{11} \text{ n cm}^{-3}$  at  $\log(T) = 9$  and to  $\simeq 6 \times 10^{12} \text{ n cm}^{-3}$  at  $\log(T) = 9.3$ . The half-life of  $^{60}\text{Fe}$  also has a steep dependence on the temperature: it remains of the order of the terrestrial value up to  $\log(T) = 8.6$  and then drops to half a year at  $\log(T) = 9$ , to  $\sim 1.5$  days at  $\log(T) = 9.2$ , and to  $\sim 14$  minutes at  $\log(T) = 9.4$ . In spite of this strong dependence of its half-life

on the temperature, and contrarily to what happens to  $^{26}\text{Al}$ ,  $^{60}\text{Fe}$  is mainly destroyed by the  $(n, \gamma)$  reaction because the  $^{60}\text{Fe}(n, \gamma)$  rate always overcomes the decay rate at the extremely high neutron densities required to produce it. A temperature of the order of 2 billion degrees represents an upper temperature limit for the synthesis of  $^{60}\text{Fe}$  because above this temperature the  $(\gamma, n)$  and the  $(\gamma, p)$  photodisintegrations of both  $^{60}\text{Fe}$  and  $^{59}\text{Fe}$  become tremendously efficient. Such an occurrence limits a possible  $^{60}\text{Fe}$  production to the He, C, and Ne burning phases.

In He burning, where the main neutron donor is the  $^{22}\text{Ne}(\alpha, n)^{25}\text{Mg}$  process, a temperature of the order of  $4 \times 10^8$  K would be required to reach the threshold neutron density of  $3 \times 10^{10} \text{ n cm}^{-3}$ . In central He burning the temperature remains well below  $3 \times 10^8$  K so that the neutron density never exceeds  $10^7 \text{ n cm}^{-3}$  and no appreciable production of  $^{60}\text{Fe}$  occurs. In shell He burning, vice versa, the temperature may raise up to and above  $4 \times 10^8$  K so that even a large amount of  $^{60}\text{Fe}$  may be synthesized. To understand its synthesis in this phase it is necessary to briefly recall a few firmly established characteristics of the shell He burning. At variance with the central H burning, where the mass size of the convective core shrinks together with the H content, central He burning is characterized by a convective core that advances progressively in mass (or remains stable at most) as the He is depleted. As a consequence, the He profile left by the central He burning shows a sharp discontinuity in correspondence to the location of the maximum size of the convective core and the He convective shell forms outside this discontinuity in a region where the He abundance is flat and equal to the one left by the H burning; since all the advanced burning phases are very rapid with respect to the shell He-burning timescale, only a modest amount of He is burnt in the shell before the core collapse so that its final abundance barely drops below 0.9 by mass fraction. The temperature at the base of this convective shell never raises enough to make the  $^{59}\text{Fe}(n, \gamma)$  process competitive with respect to the  $^{59}\text{Fe}(\beta^-)$  decay, so no  $^{60}\text{Fe}$  is synthesized by these stars. Such a feature holds up to the first mass that becomes a W-R star of the WNE/WCO kind ( $40 M_\odot$ ). In fact, these stars experience such a strong mass loss that they first lose all their H-rich envelope and then continue eroding the He core up to the moment of the core collapse. Since the properties of the He burning depend on the He core mass size, the core “feels” a progressively smaller mass as the He core reduces, and hence the mass size of the convective core reduces accordingly: a He profile is left in these stars at the central He exhaustion, and its shape will depend on the balance between the speed of the central burning and the mass-loss rate. The He convective shell forms, in these stars, within the region of variable He abundance, and hence the well-known problem arises of whether the Schwarzschild criterion or the Ledoux one must be used to determine if (and on which timescale) a convective region forms. We do not want to address this question here, mainly because a full nonlocal treatment of the mixing is still missing and only semiphenomenological (and parametric) solutions have been proposed over the years to treat these layers. We decided, on the contrary, to explore two limiting cases: one in which the Schwarzschild criterion is adopted, and a second in which the Ledoux criterion is used. Columns (8) and (9) in Table 3 show the amount of  $^{60}\text{Fe}$  that is produced in the two limiting cases: it is evident that the presence of a fully convective region largely increases the amount of  $^{60}\text{Fe}$  synthesized by the shell He burning. Typical neutron densities reached in the He shell in these very massive stars range between  $6 \times 10^{10}$  and  $1 \times 10^{12} \text{ n cm}^{-3}$ . A rather modest, but worth being mentioned, additional amount of  $^{60}\text{Fe}$  is also produced in the radiative tail of the He burning shell of the less massive stars. These

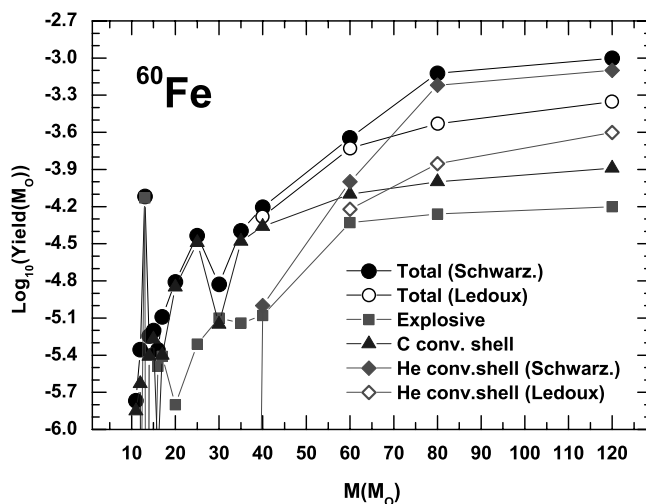


FIG. 6.— $^{60}\text{Fe}$  yields as a function of the initial mass. The filled and open circles refer to the total amount of  $^{60}\text{Fe}$  ejected as a function of the initial mass, for two different choices of the stability criterion in the He convective shell, i.e., the Schwarzschild and the Ledoux criteria, respectively. The other lines show the various contributions to the total yield. [See the electronic edition of the *Journal* for a color version of this figure.]

stars experience a significant contraction of the core (including the radiative tail of the He shell) after the end of the central oxygen burning phase that raises the temperature (and hence the neutron density) enough to allow the synthesis of some  $^{60}\text{Fe}$  (col. [7] in Table 3). As the initial mass increases, this phenomenon disappears because the region external to the CO core becomes progressively more insensitive to the evolution of the deep interior of the star (mainly because of the presence of a very active and stable C convective shell). The contribution of the He convective shell to the synthesis of  $^{60}\text{Fe}$  is shown in Figure 6 as filled rhombs when the Schwarzschild criterion is adopted (Pratzos 1989) and as open rhombs when the Ledoux criterion is adopted.

C burning behaves similarly to the He burning. In central C burning the neutron density does not exceed a few times  $10^7 \text{ n cm}^{-3}$ , so that also in this case no  $^{60}\text{Fe}$  may be produced. The main neutron donor is, once again, the  $^{22}\text{Ne}(\alpha, n)^{25}\text{Mg}$  process, and the reason why it cannot provide a high neutron rate is, in this case, the relatively low concentration of  $\alpha$ -particles provided by the  $^{12}\text{C}(^{12}\text{C}, \alpha)^{20}\text{Ne}$  reaction. In analogy with the He burning, the larger burning temperature ( $T \geq 10^9$  K) at which the shell C burning occurs, allows a much larger production of  $\alpha$ -particles that translates into a much higher neutron density and hence in a conspicuous  $^{60}\text{Fe}$  production. The typical neutron density we find ranges between  $6 \times 10^{11}$  and  $2 \times 10^{12} \text{ n cm}^{-3}$  in the mass range  $20$ – $120 M_\odot$  while it drops significantly at lower masses. The mild dependence of the neutron density at the base of the C convective shell on the initial mass (for  $M > 17 M_\odot$ ) explains why the  $^{60}\text{Fe}$  produced by the C convective shell (triangles in Fig. 6 and col. [10] in Table 3) increases only modestly with the initial mass. It must be noted, at this point, that the presence of a convective shell plays a crucial role also for the synthesis of  $^{60}\text{Fe}$ . In fact it has the double responsibility of bringing new fuel ( $\alpha$ -particles and  $^{22}\text{Ne}$ ) in the region where the active burning occurs and simultaneously of bringing the freshly made  $^{60}\text{Fe}$  outward in mass, i.e., at lower temperatures where the neutron density becomes negligible and its half-life increases substantially. The  $30 M_\odot$  model is the best example of the importance of the convective burning: in fact, the minimum in the yield of the

$^{60}\text{Fe}$  produced by the C shell (see Fig. 6) corresponding to the  $30 M_{\odot}$  model is the direct consequence of the lack of an efficient C convective shell lasting all along the advanced evolutionary phases (see the previous section).

Ne burning would produce  $^{60}\text{Fe}$  too, because of the large abundance of the  $\alpha$ -particles and neutrons provided in this case by the  $^{23}\text{Na}(\alpha, n)^{26}\text{Al}$  reaction, but the lack of an extended and stable convective shell lasting up to the moment of the explosion prevents the build up of a significant amount of  $^{60}\text{Fe}$ . In fact, the  $^{60}\text{Fe}$  produced by the advancing Ne burning shell drops quickly to zero together with the local Ne abundance because either the production channel dries up and the  $\beta^-$  decay speeds up consistently. By the way, the Ne convective shell that forms in the 14 and  $15 M_{\odot}$  after the end of the central Si burning is responsible for the strong peak in the  $^{26}\text{Al}$  yield produced by these masses (see Fig. 2), does not lead to a similar effect for the  $^{60}\text{Fe}$  because the neutron density remains too low to cross the  $^{59}\text{Fe}$  bottleneck.

The last episode of synthesis of  $^{60}\text{Fe}$  occurs when the blast wave crosses the mantle of the star on its way out, in the region where the peak temperature is of the order of  $2.2 \times 10^9$  K and hence roughly in the same region where the (explosive) synthesis of  $^{26}\text{Al}$  occurs. In most cases such a temperature is reached either at the base or within the C convective shell so that the amount of explosive  $^{60}\text{Fe}$  produced will depend on the local abundances of  $^{20}\text{Ne}$ ,  $^{12}\text{C}$ ,  $^{23}\text{Na}$ , and  $^{22}\text{Ne}$  left by the last C convective shell episode and on the final MR relation at the moment of the core collapse. The filled squares in Figure 6 and col. (11) in Table 3 show the contribution of the explosive burning to the synthesis of  $^{60}\text{Fe}$  as a function of the initial mass. Two local minima corresponding to the two inversions in the MR relation are quite evident also in this case (see the previous section). In the mass interval  $11\text{--}15 M_{\odot}$ , the explosive contribution to the synthesis of  $^{60}\text{Fe}$  is almost negligible because of the low concentration of the nuclei that are necessary for its synthesis. The  $13 M_{\odot}$  constitutes, however, a striking exception because a large amount of  $^{60}\text{Fe}$  is synthesized by the blast wave in this case. The reason is that the peak temperature of  $2.2 \times 10^9$  K occurs beyond the outer border of the C convective shell where the abundances of  $^{12}\text{C}$  and  $^{22}\text{Ne}$ , in particular, are much higher than in the C convective shell. Since such a phenomenon occurs for just a single mass, one could question its reality. A close look at the models shows that, while the radius at which the blast wave synthesizes  $^{60}\text{Fe}$  in these low-mass stars remains roughly constant ( $\sim 0.013 R_{\odot}$ ), the radius of the outer border of the last C convective shell at the moment of the core collapse shows a nonmonotonic trend with the initial mass and, in particular, a minimum value of  $0.012 R_{\odot}$  for the  $13 M_{\odot}$  occurs. Such a minimum corresponds to a local minimum in the mass size of the last C convective shell as well. It is not easy to understand why the last C convective shell has a minimum mass size for this mass because the temporal evolution and mass (and radial) extension of the various convective episodes that follow each other depend on a nonlinear interplay among various factors (the main ones being the mass sizes of both the He and the CO core and the amount of C left by the central He burning). To better assess the range of masses for which this peculiar explosive production occurs, the computation of a finer mass grid would be required: at present we can just say that it is confined somewhere between  $12$  and  $14 M_{\odot}$ . Let us finally note that no  $^{60}\text{Fe}$  is lost by the stellar wind because, in the present computations, no fraction of the He convective shell is lost through the wind during the advanced W-R phase.

The filled circles in Figure 6 and column (6) in Table 3 show the total yield of  $^{60}\text{Fe}$  as a function of the initial mass in the case

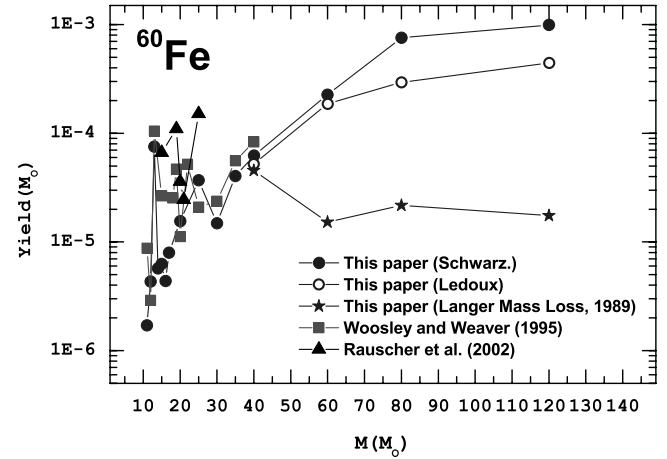


FIG. 7.—Comparison among the  $^{60}\text{Fe}$  yields provided by various authors. [See the electronic edition of the Journal for a color version of this figure.]

in which the Schwarzschild criterion is assumed in the He convective shell. Its trend obviously reflects the trends of the main contributors at the various masses. There is a global direct scaling with the initial mass and a quite monotonic behavior: the two exceptions are the  $13$  and the  $30 M_{\odot}$ . Below  $40 M_{\odot}$  the total yield is dominated by the contribution of the C convective shell while above this mass it is the He convective shell to play the major role. The explosive burning almost always plays a minor role. The open circles refer to the case in which the Ledoux criterion is assumed in the He convective shell: its contribution to the global synthesis of  $^{60}\text{Fe}$  is strongly reduced in this case.

Similarly to the  $^{26}\text{Al}$  case, the treatment of the convective layers and the cross section of the  $^{12}\text{C}(\alpha, \gamma)^{16}\text{O}$  are strong sources of uncertainty in the prediction of the  $^{60}\text{Fe}$  yield (see the previous section). The situation is even worse in this case because the cross sections of all the key processes involved in the synthesis of  $^{60}\text{Fe}$  are purely theoretical: no experimental data exist for the  $^{59}\text{Fe}(n, \gamma)$  and the  $^{60}\text{Fe}(n, \gamma)$  rates or for the dependence of their  $\beta^-$  decay on the temperature. Let us finally note that, since  $^{60}\text{Fe}$  is mainly synthesized by the C and He shells, it may well be considered a pure secondary element because both the target (Fe) and the bullet (neutrons) depend on the initial metallicity (the neutrons, in fact, mainly come from the  $^{22}\text{Ne}(\alpha, n)$  process). Therefore, the rate of this process as well as the adopted initial [CNO/Fe] ratio (scaled solar or not) will significantly influence the final  $^{60}\text{Fe}$  outcome.

$^{60}\text{Fe}$  yields have been published, as far as we know, by Timmes et al. (1995a as part of the WW95 large database) and by Rauscher et al. (2002); these are shown in Figure 7 as filled squares and filled triangles, respectively. Our yields obtained for the two extreme cases are shown as filled and open circles. For sake of completeness the yields obtained by adopting the Langer (1989) mass-loss rate are also shown (see next section). The first thing worth noting is that our yields are the only ones available above  $40 M_{\odot}$ . Second, a good overall agreement exists between the WW95 and our yields: both sets show a peak toward the lower end ( $13 M_{\odot}$  in both cases) and a minimum ( $20 M_{\odot}$  in WW95 and  $30 M_{\odot}$  in our models) that clearly indicate how the two sets of models behave similarly (at least qualitatively). As for Rauscher et al. (2002), their yields are systematically and significantly larger than both the WW95 and our yields. We do not have an definite explanation for such a difference since our models, computed with the latest input physics available today, show a remarkable agreement with

TABLE 5  
SELECTED PROPERTIES OF THE MODELS COMPUTED  
WITH THE LANGER (1989) MASS-LOSS RATE

$M_{\text{ini}}$ ( $M_{\odot}$ ) (1)	$M_{\text{end}}$ ( $M_{\odot}$ ) (2)	$M_{\text{CO}}$ ( $M_{\odot}$ ) (3)	$^{26}\text{Al}_{\text{wind}}$ ( $M_{\odot}$ ) (4)	$^{26}\text{Al}_{\text{C shell+expl.}}$ ( $M_{\odot}$ ) (5)	$^{26}\text{Al}_{\text{tot}}$ ( $M_{\odot}$ ) (6)	$^{60}\text{Fe}_{\text{tot}}$ ( $M_{\odot}$ ) (7)
40.....	6.88	5.25	2.17(-5)	1.053(-4)	1.27(-4)	4.54(-5)
60.....	6.01	4.54	7.51(-5)	4.490(-5)	1.20(-4)	1.52(-5)
80.....	6.10	4.61	1.42(-4)	1.120(-4)	2.54(-4)	2.17(-5)
120.....	6.18	4.68	3.02(-4)	4.200(-5)	3.44(-4)	1.75(-5)

the WW95 ones that have been computed with the input physics available at that time and not with the Rauscher et al. (2002) one that has probably been computed with a much closer input physics. Let us finally remark that our  $^{60}\text{Fe}$  yields already published in 2003 and 2004 (Limongi & Chieffi 2003; Chieffi & Limongi 2004) are in very close agreement with the present ones.

## 5. DEPENDENCE OF THE YIELDS ON THE MASS-LOSS RATE ADOPTED BEYOND THE WNL PHASE

In the previous sections we have discussed at some extent the yields of both the  $^{26}\text{Al}$  and  $^{60}\text{Fe}$  as a function of the initial mass, as well as their dependence on some nuclear processes and some physical phenomena (like the efficiency of the convective mixing). In this section we show how the yields of these two nuclei depend on the mass-loss rate beyond the WNL phase. As is well known, mass loss is still one of the main uncertain physical phenomena that influence the evolution of a star. To explore the influence of the mass loss in the WNE+WCO phases we have recomputed the evolution of the stellar models that enter the WNE (i.e., stars in the range 40 to 120  $M_{\odot}$ ) by adopting the mass-loss rate proposed by Langer (1989) and widely adopted in the past. This older mass-loss rate is much stronger than the Nugis & Lamers (2000) one, and it scales as  $M^{2.5}$ , so that all the very massive models tend now to converge toward a similar quite small final mass (col. [2] in Table 5). Moreover, since such a strong reduction of the total mass occurs during the central He burning, all these models tend to have a quite similar CO core mass (col. [3] in Table 5) and hence quite similar advanced burning phases. This is the reason why the  $^{26}\text{Al}$  and  $^{60}\text{Fe}$  produced by the advanced burnings (hydrostatic plus explosive) tend to become quite insensitive to the initial mass (cols. [5] and [7] in Table 5). Of course, the  $^{26}\text{Al}$  lost by the wind (col. [4] in Table 5) preserves, on the other hand, a strong dependence on the initial mass because it is ejected in the earliest phases of the evolution of these stars. Note that the  $^{26}\text{Al}$  ejected by the wind is slightly larger in the Langer case because a larger fraction of the He core is ejected before being reached by the He burning. The total amount of  $^{26}\text{Al}$  obtained by adopting the Langer (1989) mass-loss rate (col. [4] in Table 5) is compared to the one obtained by adopting the Nugis & Lamers (2000) mass-loss rate in Figure 8 (left axis). A similar comparison for the  $^{60}\text{Fe}$  is shown in the same figure (right axis). It is clear from these comparisons that while the  $^{26}\text{Al}$  yield is reduced by roughly a factor of 2, the  $^{60}\text{Fe}$  one shows a dramatic dependence on the adopted mass-loss rate. The reason is that the  $^{60}\text{Fe}$  yield is dominated, in these very massive stellar models, by the He convective shell contribution (see the previous section), and the very strong mass loss implied by the Langer prescription completely kills such a contribution because it reduces enormously the final CO core mass. Hence, also the stability criterion adopted in the He convective shell does not play any significant role in this case.

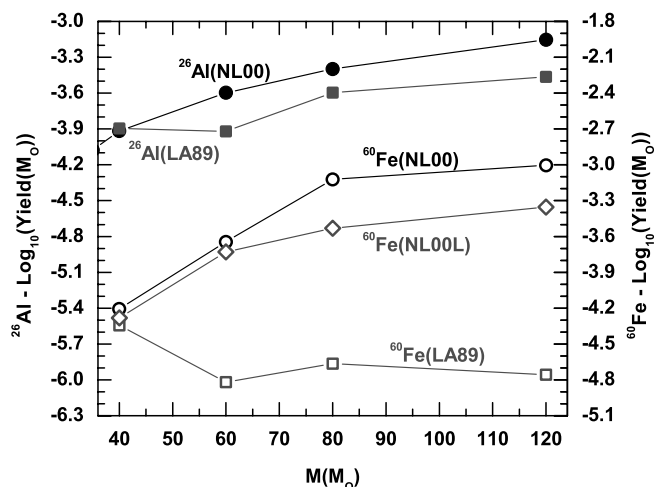


FIG. 8.— $^{26}\text{Al}$  yields (left axis) as a function of the initial mass: the filled squares refer to the models computed with the Langer (1989) mass-loss rate (LA89), while the filled circles refer to the models computed with the Nugis & Lamers (2000) mass-loss rate (NL00).  $^{60}\text{Fe}$  yields (right axis) as a function of the initial mass: the red open squares refer to the models computed with the Langer (1989) mass-loss rate (LA89), and the open circles and the open rhombs refer to the models computed with the Nugis & Lamers (2000) mass-loss rate adopting the Schwarzschild (NL00) and the Ledoux (NL00L) criteria in the He convective shell, respectively. [See the electronic edition of the Journal for a color version of this figure.]

## 6. COMPARISON WITH THE OBSERVATIONS

The clumpy and patchy distribution of the  $^{26}\text{Al}$  in the Galactic plane shown by COMPTEL, coupled to the strong correlation between its all-sky map and the 53 GHz free-free emission map, point toward a massive star parent for the  $^{26}\text{Al}$ , and more specifically, toward the subset of massive stars that are also responsible for the Lyman continuum photons that power the ionization of the interstellar medium. By comparing the 53 GHz free-free emission to the  $^{26}\text{Al}$  decay map, Knödseder (1999) determined also that the scaling factor between the 1.8 MeV  $\gamma$ -ray line ( $\gamma_{1.8}$ ) flux and the Lyman continuum photons (LCP) flux remains roughly constant all over the Galactic plane. He quantified this occurrence by identifying the average amount of  $^{26}\text{Al}$  ( $Y_{26}^{07V} = 10^{-4} M_{\odot}$ ) that must be associated to the LCP flux ( $Q_0$ ) of an equivalent O7 V star [ $\log(Q_0) = 49.05$ ] in order to obtain the observed correlation between the two aforementioned all-sky maps (see Knödseder 1999 for details). For reasons of convenience we prefer to reinterpret these data in terms of number of  $\gamma_{1.8}$  photons per ionizing photon (GPL); this number, which we name for convenience  $R_{\text{GXL}}$ , is equal to  $1.25 \times 10^{-11}$  GPL. Let us recall once again that the determination of  $R_{\text{GXL}}$  does not require any explicit assumption about the sources of the ionizing photons and of the  $^{26}\text{Al}$ , but only that the  $^{26}\text{Al}$  nuclei and the LCP share the same spatial distribution (Knödseder 1999).

We have discussed in the previous sections essentially three sets of models that differ because of the mass-loss rate adopted in the WNE+WCO phases and because of the stability criterion adopted in the He convective shell. For the sake of clarity, we refer to the set of models computed by adopting the Nugis & Lamers (2000) mass-loss rate in the WNE+WCO phases and the Schwarzschild criterion in the He convective shell as the NL00 models, and the ones computed with the same mass-loss rate but the Ledoux criterion in the He convective shell as the NL00L models; the set computed by adopting the Langer (1989) mass-loss rate will be referred to as the LA89 models. Since all these different choices concern only stars more massive than 35  $M_{\odot}$ ,

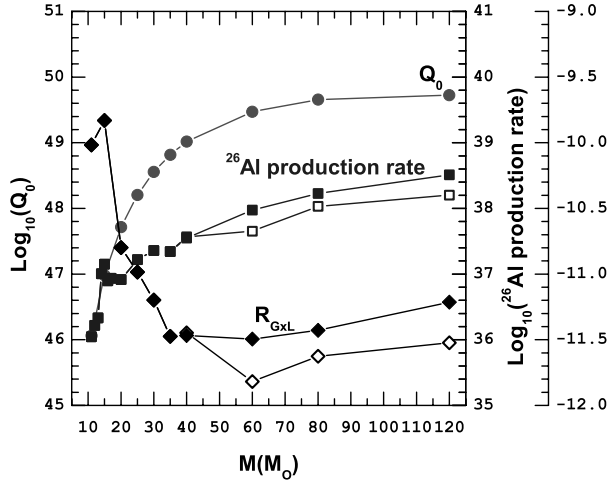


FIG. 9.—Lyman continuum photons per second ( $Q_0$ ) (filled circles, left axis) and average  $^{26}\text{Al}$  production rate (filled and open squares for the NL00 and LA89 models, respectively; first right axis) as a function of the initial mass. The rhombs refer to the number of  $\gamma_{1.8}$  photons per ionizing photon ( $R_{\text{GxL}}$ , second right axis). In particular the filled and open rhombs refer to the NL00 and LA89 models, respectively. [See the electronic edition of the Journal for a color version of this figure.]

all these sets share the same stellar models between 11 and  $35 M_{\odot}$ .

From the theoretical side we can easily determine the  $R_{\text{GxL}}$  factor(s) for our grid of models. Let us recall that at the base of this derivation there is the usual assumption of a steady state condition, i.e., of the equivalence between destruction and production rates: this implies that the observed decay rate of the  $^{26}\text{Al}$  is equal to the average ejection rate of this nucleus from the currently evolving stars. We have estimated the number of Lyman continuum photons produced by each of our models by means of Table 3 of Schaerer & de Koter (1997); the two following relations provide both the average  $\log(Q_0)$  and the lifetime of a star as a function of the initial mass (for our grid of models):

$$\log_{10}(Q_0) = 34.4906 + 14.90772 \times \log_{10}(M) - 3.64592 \times \log_{10}(M)^2 \quad (\text{LCP}) \text{ s}^{-1},$$

$$\log_{10}(t) = 9.598 - 2.879 \times \log_{10}(M) + 0.6679 \times \log_{10}(M)^2 \quad (\text{yr}).$$

Note that these relations are obviously identical for the three sets of models. Figure 9 shows the trend of both  $\log_{10}(Q_0)$  (filled circles, left axis) and the average  $^{26}\text{Al}$  production rate (first right axis) with the initial mass. The filled and open squares refer to the NL00 and the LA89 models, respectively. By the way, the average  $^{26}\text{Al}$  production rate is simply the total amount of  $^{26}\text{Al}$  produced by a star divided by its lifetime. The  $R_{\text{GxL}}$  factor per each stellar mass is also shown in the same figure and its scale is on the second right axis. The filled and open rhombs refer, respectively, to the NL00 and LA89 cases.  $R_{\text{GxL}}$  remains roughly constant above  $30 M_{\odot}$  because both  $\log_{10}(Q_0)$  and the  $^{26}\text{Al}$  production rate run almost parallel; below this mass, on the other hand, the Lyman continuum photons drop down faster than the  $^{26}\text{Al}$  production rate, so that  $R_{\text{GxL}}$  increases significantly. Note that  $R_{\text{GxL}}$  varies by roughly a factor of 2 between the NL00 and the LA89 stellar models.

The data shown in Figure 9 cannot be directly used to interpret the observed Galactic value of  $R_{\text{GxL}}$  because stars of different

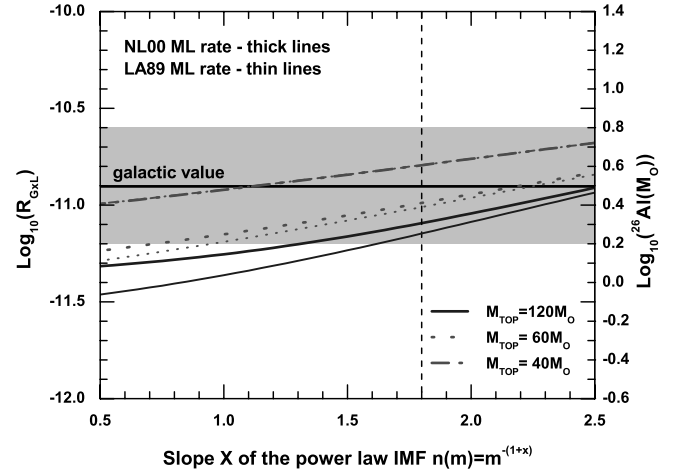


FIG. 10.— $R_{\text{GxL}}$  as a function of the IMF slope  $x$  for three different values of the IMF upper mass limit  $M_{\text{top}}$ , namely, 40 (dashed line), 60 (dotted line), and  $120 M_{\odot}$  (solid line). The thick and thin lines refer to the NL00 and the LA89 models, respectively. The corresponding total amount of  $^{26}\text{Al}$  present in the Galaxy obtained by adopting  $Q_{\text{MW}} = 3.5 \times 10^{53} \text{ photons s}^{-1}$  (see text) is shown on the right axis. The horizontal thick solid line marks the observed Galactic value derived by Knödseder (1999), but expressed in terms of  $R_{\text{GxL}}$ , while the shaded area reflects the range of values that correspond to an uncertainty of a factor of 2 in the observed value. The vertical black dashed line marks a conservative representation of the actual IMF slope of massive stars,  $x = 1.8$ , as reported by Kroupa & Weidner (2003) and Kroupa (2004). [See the electronic edition of the Journal for a color version of this figure.]

masses contribute simultaneously to both the LCP and the  $\gamma_{1.8}$  fluxes, and hence a proper initial mass function (IMF) must be taken into account. The IMF is usually expressed as a power law, namely,

$$n(m) = Km^{-(1+x)},$$

where  $n(m)$  is the number of stars of mass  $m$ . The constant  $K$  is fixed by the condition

$$N_{\text{tot}} = \int_{M_{\text{bottom}}}^{M_{\text{top}}} Km^{-(1+x)} dm = 1,$$

where  $M_{\text{bottom}}$  and  $M_{\text{top}}$  represent the limiting masses that bracket the range of the stars that explode as core-collapse supernovae. As for the lowest mass that explodes as a core-collapse supernova, we have adopted the smallest star in our grid, i.e., the  $11 M_{\odot}$ . One could question whether even less massive stars explode as core-collapse supernovae, but practically this does not influence the computation of the  $R_{\text{GxL}}$  parameter because below  $11 M_{\odot}$  both the LCP and the  $^{26}\text{Al}$  drop practically to zero. On the other hand, the choice of the upper limit may play a role. Figure 10 shows the theoretical  $R_{\text{GxL}}$  for a range of possible values of the power law slope,  $x$ , and three different values of the upper mass limit  $M_{\text{top}}$ . The solid, dotted, and dashed lines refer to three different choices of the upper mass limit: 120, 60, and  $40 M_{\odot}$ , respectively. The thick and thin lines refer to the NL00 and LA89 models, respectively. It is quite evident that, fortunately,  $R_{\text{GxL}}$  does not depend significantly on the adopted mass-loss rate, and that the dependence on  $M_{\text{top}}$  is quite modest; in fact, even a drastic change of  $M_{\text{top}}$  from, e.g., 120 to  $40 M_{\odot}$ , affects  $R_{\text{GxL}}$  by no more than a factor of 2. The reason for such a low dependence of  $R_{\text{GxL}}$  on  $M_{\text{top}}$  is that above  $30 M_{\odot}$  the ratio between the  $^{26}\text{Al}$  production rate and Lyman continuum luminosity remains roughly constant (see Fig. 9) for all sets of models.

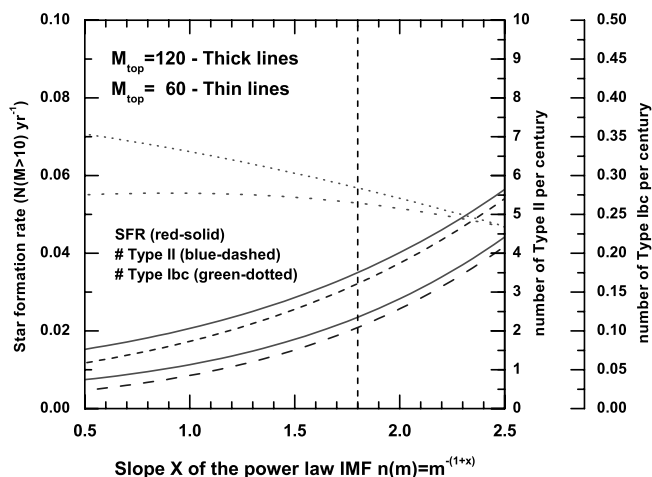


FIG. 11.—Star formation rate (number of stars greater than  $10 M_{\odot}$  per year; left axis, solid lines), number of Type II (first right axis, dashed lines) and Type Ibc (second right axis, dotted lines) supernovae per century as a function of the IMF slope  $x$  for two choices of the upper mass limit  $M_{\text{top}}$  of the IMF, namely,  $60 M_{\odot}$  (thin lines) and  $120 M_{\odot}$  (thick lines). A total Galactic Lyman continuum luminosity  $Q_{\text{MW}} = 3.5 \times 10^{53}$  photons  $\text{s}^{-1}$  has been assumed (see text). The vertical dashed line has the same meaning as in Fig. 10. [See the electronic edition of the Journal for a color version of this figure.]

The horizontal thick solid black line marks the observed Galactic value derived by Knödseder (1999), but expressed in terms of  $R_{\text{GxL}}$ , while the shaded area reflects the range of values that correspond to an uncertainty of a factor of 2 in the observed value. Kroupa & Weidner (2003) and Kroupa (2004) have recently rediscussed the IMF slope for massive stars and came to the conclusion that it must be larger than, at least,  $x = 1.8$ . If we take this specific value (Fig. 10, thin vertical dashed line) as a conservative representation of the actual IMF slope of these stars, it turns out that a good fit to the Galactic  $R_{\text{GxL}}$  exists for any  $M_{\text{top}}$  mass ranging between, at least, 120 and  $40 M_{\odot}$  and both sets of models. The fit improves for steeper IMF slopes. We therefore conclude that both the NL00 and the LA89 sets of models can naturally explain and reproduce the constant Galactic  $R_{\text{GxL}}$ .

The good fit to this parameter, however, does not carry any information, by itself, about the total amount of  $^{26}\text{Al}$  present in our Galaxy. In order to determine such an amount by means of  $R_{\text{GxL}}$ , it is necessary to know the total Lyman continuum luminosity provided by our Galaxy ( $Q_{\text{MW}}$ ). Once this value is known, the global  $^{26}\text{Al}$  production rate,  $P_{\text{MW}}^{26\text{Al}}$ , is given by  $P_{\text{MW}}^{26\text{Al}} = Q_{\text{MW}} \times R_{\text{GxL}}$  and the present steady state abundance of  $^{26}\text{Al}$  in our Galaxy would be given by  $P_{\text{MW}}^{26\text{Al}} \times \tau_{\text{dec}}^{26\text{Al}}$ .

Recent determinations of the Galactic Lyman continuum luminosity range between  $Q_{\text{MW}} = 3.5 \times 10^{53}$  photons  $\text{s}^{-1}$  (Bennett et al. 1994) and  $Q_{\text{MW}} = 2.6 \times 10^{53}$  photons  $\text{s}^{-1}$  (McKee & Williams 1997) with about 50% uncertainty in both cases (see the cited papers for details). If one adopts the highest value (Bennett et al. 1994), an IMF slope  $x = 1.8$  and  $M_{\text{top}} = 120 M_{\odot}$ , the present steady state abundance of  $^{26}\text{Al}$  in our Galaxy would amount to  $1.97 M_{\odot}$  for the NL00 models and to  $1.70 M_{\odot}$  for the LA89 case. Figures 10 (right scale) and 11 show the trends of the  $^{26}\text{Al}$  abundance, of the star formation rate (SFR), of the number of Type II supernovae and of the Type Ibc supernovae as a function of the slope  $x$  for a  $Q_{\text{MW}} = 3.5 \times 10^{53}$  photons  $\text{s}^{-1}$ . In Figure 11 the thick lines refer to an  $M_{\text{top}} = 120 M_{\odot}$ , while the thin lines refer to an  $M_{\text{top}} = 60 M_{\odot}$ . Since all these relations scale linearly with  $Q_{\text{MW}}$ , the adoption of the value provided by (McKee & Williams 1997) would simply imply a downward scaling by a factor equal to 2.6/3.5. The quantities shown in Figure 11 obvi-

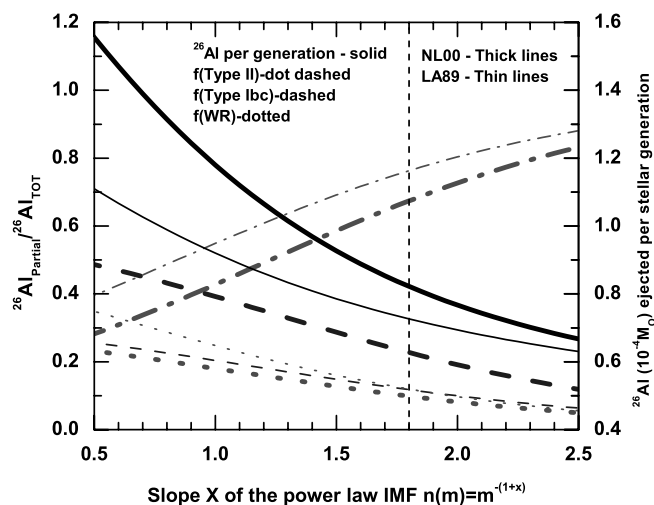


FIG. 12.—Total amount of  $^{26}\text{Al}$  ejected by a generation of massive stars in the range 11– $120 M_{\odot}$  (solid lines, right axis) as a function of the slope  $x$  of the IMF. Percentage contribution of the Type II supernovae (dot-dashed lines), the Type Ibc supernovae (dashed lines), and the Wolf-Rayet stars (dotted lines) to the synthesis of  $^{26}\text{Al}$  as a function of the IMF slope  $x$ . The thick and thin lines refer to the NL00 and LA89 models, respectively. The vertical dashed line has the same meaning as in Fig. 10. [See the electronic edition of the Journal for a color version of this figure.]

ously do not depend at all either on the adopted mass loss beyond the WNL phase or on the stability criterion adopted in the He convective shell. Figure 12 shows the total amount of  $^{26}\text{Al}$  ejected by a stellar generation (solid lines, right axis) together with the percentage contributions of the Type II supernovae (dot-dashed lines), the Type Ibc supernovae (dashed lines), and the W-R stars (dotted lines), all as a function of the IMF slope  $x$ : the thick and thin lines refer to the NL00 and the LA89 cases, respectively. The observed trends may be readily understood by recalling that (1) the LA89 models predict systematically less  $^{26}\text{Al}$  than the NL00 ones (see Table 5) because of the reduced production both in the C convective shell and Ne explosive burnings (see the previous section) and (2) the total amount of  $^{26}\text{Al}$  ejected by the Type II supernovae is identical in both sets because they share the same stellar models below  $40 M_{\odot}$ . Since the integration over the IMF may depend on the adopted upper mass limit ( $M_{\text{top}}$ ), we show in Figures 13 (for the NL00 case) and 14 (for the LA89 case) the

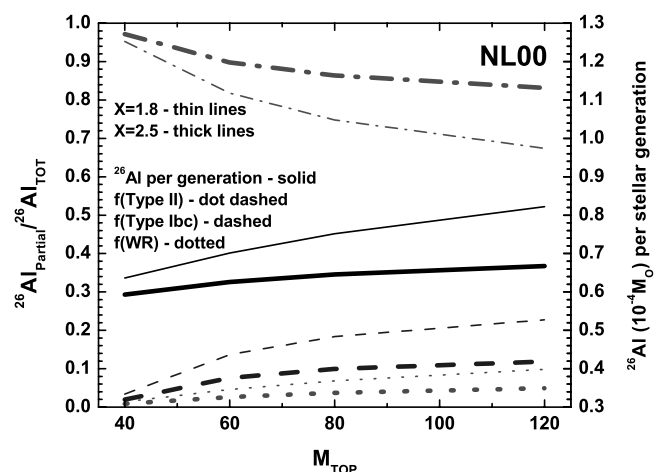


FIG. 13.—Same quantities shown in Fig. 12 as a function of  $M_{\text{top}}$  for the NL00 models and two specific slopes of the IMF, namely,  $x = 1.8$  and  $x = 2.5$ . [See the electronic edition of the Journal for a color version of this figure.]

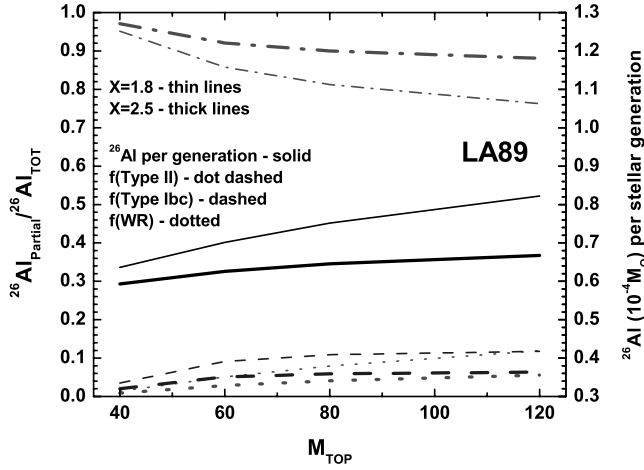


FIG. 14.—Same as Fig. 13, but for the LA89 models. [See the electronic edition of the Journal for a color version of this figure.]

same quantities shown in Figure 12 as a function of  $M_{\text{top}}$  and two specific IMF slopes, i.e.,  $x = 1.8$  and  $x = 2.5$ . Both these Figures clearly show that, independently of  $M_{\text{top}}$  and of the mass-loss rate adopted beyond the WNL stage, the largest contribution to the total  $^{26}\text{Al}$  produced by a stellar generation comes from the Type II supernovae, while both the W-R stars and the Type Ibc supernovae contribute at most (compressively) for a 30% in the most favorable case. The present result, i.e., that most of the  $^{26}\text{Al}$  comes from the Type II supernovae must be interpreted as a property of our sets of models. We have already shown in Figure 5 that the yields produced by different authors differ significantly even in the mass range they share; it is therefore very probable that they could have been different also in the mass interval not explored by other groups so that even the relative contributions of the various mass intervals could change significantly from one author to another. In other words, it would be a mistake to use a set of models that extend only up to  $30\text{--}40 M_{\odot}$  to infer the  $^{26}\text{Al}$  produced by a generation of massive stars basing such a choice on the properties of the present models. It is not known a priori what role that more massive stars would play in other sets of models. In this respect it is of overwhelming importance that other groups compute grid of models that are extended in mass at least as much as in the present ones, because only a comparison between independent computations would allow a better understanding of the role really played by the various mass intervals to the global budget of the  $^{26}\text{Al}$ . It goes without saying that the same holds for the  $^{60}\text{Fe}$ .

Both *RHESSI* and *SPI* (*INTEGRAL*) have reported a measurement of the  $^{60}\text{Fe}/^{26}\text{Al}$  flux ratio toward the central radiant of our Galaxy (see the introduction). The latest values, at the time of writing, are  $(0.17 \pm 0.05)$  (*RHESSI*; Smith 2006) and  $(0.11 \pm 0.03)$  (*SPI*; Harris et al. 2005). Since these experimental data show a compatibility range around  $^{60}\text{Fe}/^{26}\text{Al} = 0.14$ , we decided to tentatively (and arbitrarily) adopt this value as representative of both the experiments and to consider as a typical error the semidifference between the quoted values. This representative value is shown as a horizontal black thick line in Figure 15, while the two experimental values are shown as thin black solid lines in the same figure. Figure 15 also shows our theoretical predictions for the three sets of models, namely, the NL00 (solid line), the NL00L (dashed line), and the LA89 (dotted line) and  $M_{\text{top}} = 120 M_{\odot}$ . This figure shows that the NL00 models predict a  $^{60}\text{Fe}/^{26}\text{Al}$  flux ratio too large for any slope in the explored range. Such a large flux ratio is due to the very large amount of  $^{60}\text{Fe}$  produced in the

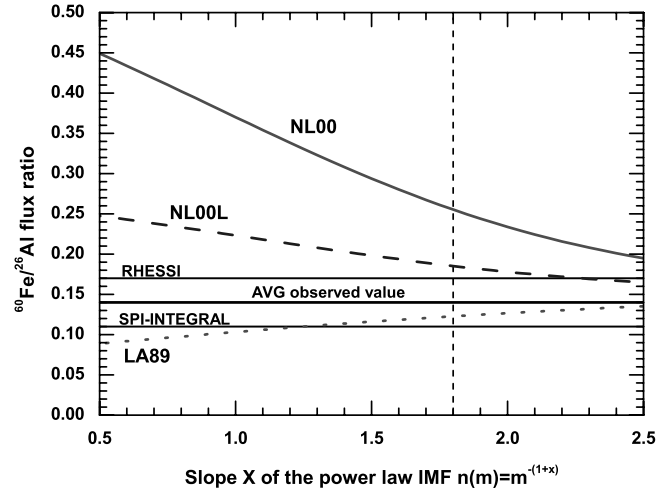


FIG. 15.—Theoretical  $^{60}\text{Fe}/^{26}\text{Al}$   $\gamma$ -ray line flux ratio as a function of the IMF slope  $x$ , for the three sets of models, namely, NL00 (solid line), NL00L (dashed line), and LA89 (dotted line). The thick horizontal black solid line shows the value averaged between the detections reported by *RHESSI* and *INTEGRAL* SPI (thin solid lines) and taken as a representative value for both the experiments. [See the electronic edition of the Journal for a color version of this figure.]

He convective shell in stars more massive than  $35 M_{\odot}$ . The adoption of the Ledoux criterion in the He convective shell significantly dumps out the  $^{60}\text{Fe}$  production in this region so that the theoretical flux ratio reduces somewhat although it remains larger than the observed value. The fit improves as the IMF slope increases because the contribution of the more massive stars reduces correspondingly. The LA89 models, on the other hand, predict an  $^{60}\text{Fe}/^{26}\text{Al}$  flux ratio in excellent agreement with the observed value over a very large range of IMF slopes, and this is the consequence of the very strong mass loss that prevents either the production of  $^{60}\text{Fe}$  in the He convective shell and reduces also its production in the C convective shell and in the Ne explosive burning. Figure 16 shows, for two selected IMF slopes, the dependence of this flux ratio on  $M_{\text{top}}$ . Only the NL00 models show a strong dependence of

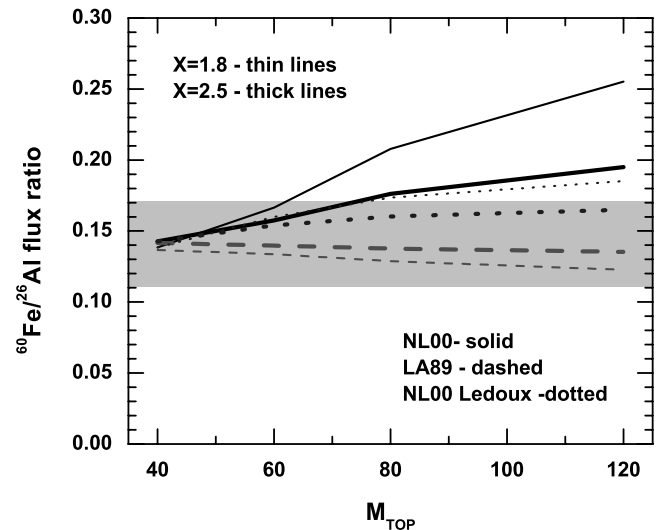


FIG. 16.—Theoretical  $^{60}\text{Fe}/^{26}\text{Al}$   $\gamma$ -ray line flux ratio as a function of  $M_{\text{top}}$  for two selected IMF slopes, namely,  $x = 1.8$  (thin lines) and  $x = 2.5$  (thick lines). The solid, dotted, and dashed lines refer to the NL00, NL00L and LA89 models, respectively. [See the electronic edition of the Journal for a color version of this figure.]

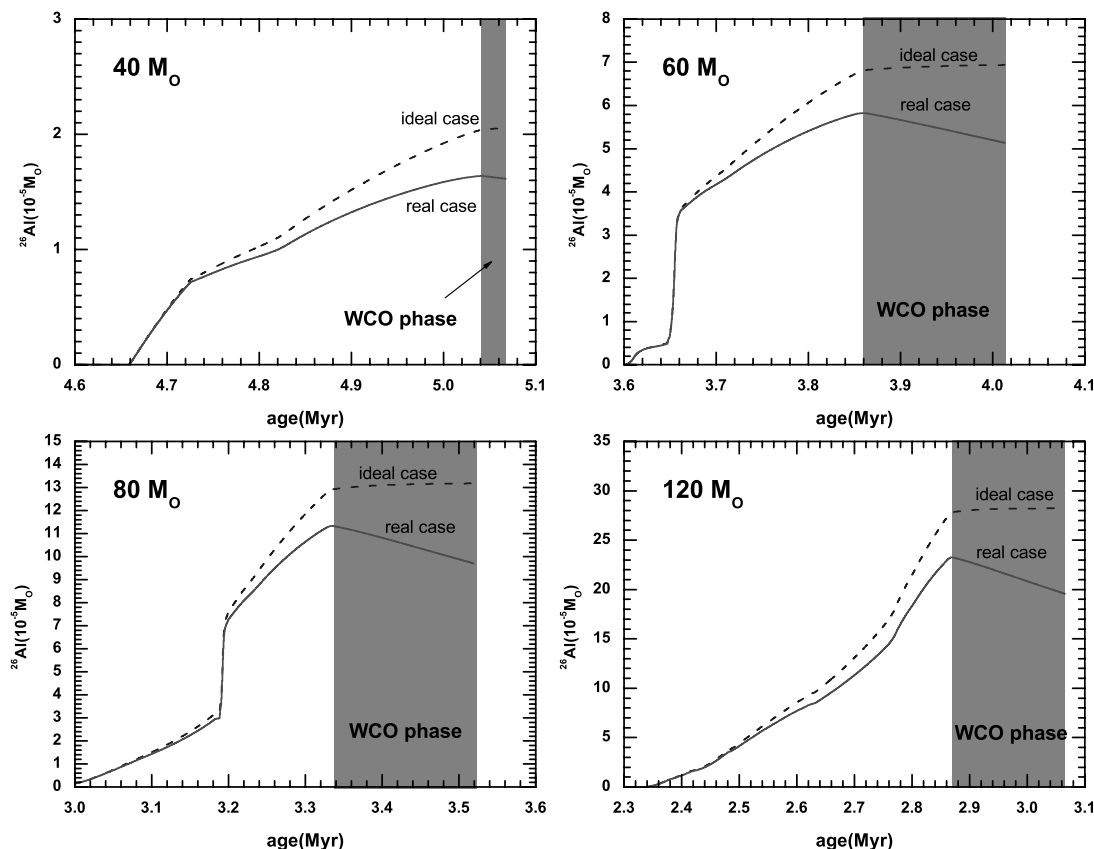


FIG. 17.—Cumulative abundance of  $^{26}\text{Al}$  present in the ejecta as a function of the age of the star. The four panels refer to the 40 (top left), 60 (top right), 80 (bottom left), and 120  $M_{\odot}$  (bottom right). The thick dashed lines show the case in which the  $^{26}\text{Al}$  is assumed to accumulate in the interstellar medium without decaying; the red solid thick lines represent the real total amount of  $^{26}\text{Al}$  one would find in the interstellar medium as a function of time, taking into account that the  $^{26}\text{Al}$  starts to decay as soon as it is ejected into the interstellar medium. The gray areas mark the temporal phase in which each star appears as a WCO star. [See the electronic edition of the *Journal* for a color version of this figure.]

the flux ratio on  $M_{\text{top}}$  and this is due to the fact that this is the only set for which a substantial contribution to the  $^{60}\text{Fe}$  comes from the stars more massive than 40  $M_{\odot}$ .

A paper devoted to the presentation of a new generation of  $^{26}\text{Al}$  yields cannot escape the temptation to reanalyze the fit to  $\gamma^2$  Velorum, the closest W-R star (WR 11) currently known. As far as we know, the latest very detailed and comprehensive analysis of this W-R star has been presented by Oberlack et al. (2000), and we refer the reader to this paper and to the references therein for a detailed discussion of both the observational aspects and the theoretical problems involved in the interpretation of this star (either in the single and binary stars scenarios). Here it suffices to say that the typical initial mass quoted for this star is  $60 \pm 15 M_{\odot}$ , that its initial metallicity was very probably solar, and that the binary system is wide enough that probably the evolution of  $\gamma^2$  Velorum was not affected much by the binarity environment. No  $^{26}\text{Al}$  has been detected around this star, but an upper limit of  $6.3^{+2.1}_{-1.4} \times 10^{-5} M_{\odot}$  has been derived by Oberlack et al. (2000). This value represents a problem because the theoretical models predict a much larger amount of  $^{26}\text{Al}$ . Meynet et al. (1997) find that a 60  $M_{\odot}$  solar metallicity star ejects  $1.49 \times 10^{-4} M_{\odot}$  of  $^{26}\text{Al}$  through the wind, while Palacios et al. (2005) quote a value of  $1.3 \times 10^{-4} M_{\odot}$  for the same initial mass; the older models by Langer et al. (1995) also predict an amount of  $^{26}\text{Al}$  equal to  $1.2 \times 10^{-4} M_{\odot}$  for a 50  $M_{\odot}$  star. Further, for a mass as low as 40  $M_{\odot}$  the models predict rather large values that are only barely compatible with the quoted upper limit:  $5.5 \times 10^{-5} M_{\odot}$  (Meynet et al. 1997) and  $5.09 \times 10^{-5} M_{\odot}$  (Langer et al. 1995). Such a failure in repro-

ducing the closest W-R star is very embarrassing because this is a member of the class of stars that are very probably responsible for the production of the bulk of the  $^{26}\text{Al}$  currently in the disk of our Galaxy. An inspection of Table 3 shows that the wind component of the  $^{26}\text{Al}$  yield in our models is roughly a factor of 2 lower than that obtained by the other authors, so that a large part of the discrepancy is removed. In addition to this, there is another important point that has been neglected up to now: the timescale over which the  $^{26}\text{Al}$  is injected into the interstellar medium. Figure 17 shows the cumulative abundance of  $^{26}\text{Al}$  present in the ejecta as a function of the age of the star and the four panels refer to the 40, 60, 80, and 120  $M_{\odot}$ : the dashed thick lines show the case in which the  $^{26}\text{Al}$  is assumed to accumulate in the interstellar medium without decaying (unrealistic, but usually adopted, ideal case in which the  $^{26}\text{Al}$  is assumed to start decaying after it has been completely ejected) while the solid thick lines represent the real total amount of  $^{26}\text{Al}$  one would find in the interstellar medium as a function of time (taking into account the fact that the  $^{26}\text{Al}$  starts to decay as soon as it is ejected in the interstellar medium). The gray areas mark the temporal phase in which each star appears as a WCO star. If  $\gamma^2$  Velorum is now just at the beginning of its WCO phase (the worst case because the *real*  $^{26}\text{Al}$  abundance is at its maximum) the predicted amount of  $^{26}\text{Al}$  would be 15%–20% smaller than the value shown in Table 3 for masses in the range 40–120  $M_{\odot}$ . In particular, an abundance of  $5.82 \times 10^{-5} M_{\odot}$  is predicted in the interstellar medium in the case of a 60  $M_{\odot}$  model, a value well below the upper limit quoted at present. This means that at least the full range of masses between 40 and 60  $M_{\odot}$  is



now compatible with the observed upper limit. There is even room for an initial mass larger than  $60 M_{\odot}$ . We cannot be more precise at the moment because our nearest grid mass is the  $80 M_{\odot}$ . The adoption of the LA89 models would not change these results appreciably. Hence we conclude that a proper treatment of the injection of the  $^{26}\text{Al}$  ejected into the interstellar medium coupled to our new yields removes the long-standing discrepancy between the upper limit quoted for  $\gamma^2$  Velorum and the theoretical predictions.

## 7. CONCLUSIONS

We have extensively discussed the production sites of the two  $\gamma$ -ray emitters  $^{26}\text{Al}$  and  $^{60}\text{Fe}$  over the range of massive stars that may contribute significantly to either the production of these nuclei and to the Lyman continuum luminosity, i.e., the range 11–120  $M_{\odot}$ . These theoretical predictions fully cover all the evolutionary phases from the pre-main-sequence to the explosive burnings. At variance with current ideas,  $^{26}\text{Al}$  is mainly produced by the Ne/C explosive burning over most of the mass interval analyzed. The main production site of the  $^{60}\text{Fe}$ , conversely, strongly depends on the adopted mass-loss rate. In the LA89 case the main  $^{60}\text{Fe}$  producer is always the C convective shell while in the NL00 case the main producer is still the C convective shell for masses lower than  $40 M_{\odot}$ , while above this mass a strong contribution comes from the He convective shell. Since the He convective shell forms, in these stars, in a region where a gradient in the He abundance is present, its contribution to the synthesis of  $^{60}\text{Fe}$  depends significantly on the adopted stability criterion (Schwarzschild or Ledoux). We have used these yields to address the problem of the diffuse abundances of  $^{26}\text{Al}$  and  $^{60}\text{Fe}$  in the Galaxy.

The discovery of an almost constant flux ratio all over the Galactic disk between the Lyman continuum photons (derived from the 53 GHz free-free emission all-sky map) and the  $\gamma_{1.8}$  MeV line (that we express as  $R_{\text{GXL}}$ , number of  $\gamma_{1.8}$  MeV photons per Lyman continuum photon [GPL]), plus the recently determined  $^{60}\text{Fe}/^{26}\text{Al}$  flux ratio toward the inner radiant of the Galaxy, constitute in our opinion the two key experimental data a set of models must satisfy. The reason is that once they are assumed to be equally spatially distributed, their ratio is independent on their spatial distribution. In addition to that, the highly uncertain SFR fortunately does not play any role in these ratios (once a steady state is assumed). The experimental value of the  $R_{\text{GXL}}$  parameter has been determined by Knödseder (1999) (even if in different units) to be  $\log(R_{\text{GXL}}) = -10.9 \pm 0.3$ , while the value of the  $^{60}\text{Fe}/^{26}\text{Al}$  flux ratio (averaged between the *RHESSI* and *SPI* values) is of the order of  $0.14 \pm 0.03$ . As for the first ratio,  $R_{\text{GXL}}$ , its constancy along the Galactic longitude could hide additional information. Different longitudes probably map combinations of different stellar populations (the smallest longitudes probably mapping the region with the highest average metallicity): hence the constancy of  $R_{\text{GXL}}$  could imply a low dependence of this ratio on the initial metallicity. The same argument does not hold for the  $^{60}\text{Fe}/^{26}\text{Al}$  flux ratio because in this case we just have one integrated measure toward the central radiant of the Galaxy.

We have shown that the observed  $R_{\text{GXL}}$  may be reproduced fairly well for a variety of slopes of the IMF and both sets of models, namely, the NL00 and the LA89 ones. If we focus on a specific slope, e.g.,  $x = 1.8$  (a value widely accepted to be reasonable for these massive stars) a maximum discrepancy of 0.2 dex is obtained, independently of the adopted  $M_{\text{top}}$  and mass-loss rate beyond the WNL phase. The fit even improves for steeper slopes. Within our sets of models,  $^{26}\text{Al}$  is mainly produced by stars less massive than, say,  $35 M_{\odot}$ , the total contribution of the more mas-

sive stars (through the wind of the W-R stars plus the Type Ibc supernovae) never exceeding 30% of the total. Also this result depends only moderately on the adopted mass-loss rate beyond the WNL phase and on  $M_{\text{top}}$ .

The theoretical  $^{60}\text{Fe}$  yield, on the contrary, strongly depends on the mass-loss rate adopted in the WNE+WCO phases mainly because mass loss controls the amount of  $^{60}\text{Fe}$  produced in the He convective shell of the stars more massive than  $35 M_{\odot}$  during the very latest phases that precede their final collapse. Depending on the adopted mass-loss rate, the predicted  $^{60}\text{Fe}/^{26}\text{Al}$  flux ratio may range between 0.12 and 0.25 for a slope  $x = 1.8$ . The models that better reproduce the observed ratio ( $\simeq 0.14$ ) are the LA89 ones since the very strong mass-loss rate proposed by Langer (1989) completely dumps out the contribution of the He convective shell and also reduces the contribution of the C convective shell because of the much smaller CO core mass. The dependence of the  $^{60}\text{Fe}/^{26}\text{Al}$  flux ratio on both the IMF slope and  $M_{\text{top}}$  is negligible in this case because of the overall modest contribution of the stars more massive than  $35 M_{\odot}$  to the global budget of the  $^{60}\text{Fe}$ . The worst fit is obtained for the NL00 models since in this case either a strong contribution to the total yield comes from the He convective shell and also the contribution from the C convective shell is larger because the mass size of the CO core is definitely much large in this case. A steep IMF plus an  $M_{\text{top}}$  not larger than, say,  $60 M_{\odot}$  could anyway reconcile also this set of models with the observed flux ratio.

Of course many other uncertainties affect both yields, and we have shown in this paper how the  $^{26}\text{Al}$  yield depends, e.g., on several cross sections, the initial abundances, and the size of the H convective core. Also, a distortion of the IMF toward the highest masses could lead, in practice, to a steepening of the slope. It must also be noted that all the present results have been obtained with solar metallicity stars while very probably at least the inner Galaxy has an average metallicity larger than solar. We actually do not know how the metallicity influences the yields of the  $^{26}\text{Al}$  and the  $^{60}\text{Fe}$ , and hence we leave such an exploration to another paper. The dependence of the  $^{26}\text{Al}$  wind component on the initial metallicity has been already discussed in a number of papers (Prantzos 1991; Meynet & Arnould 1993; Meynet et al. 1997), but unfortunately such a dependence is not representative of the global trend because we have shown in this paper that the  $^{26}\text{Al}$  present in the wind always represents a modest contribution to the total budget of the  $^{26}\text{Al}$ .

The determination of the total amount of  $^{26}\text{Al}$  present in the Galaxy requires the knowledge of an additional quite uncertain parameter, i.e., the SFR. Such a quantity is usually determined by means of either the number of core-collapse supernovae per unit time or the total Lyman continuum luminosity of the Galaxy. Since it would be desirable to have a SFR linked as strongly as possible to the stars that mainly contribute to the Lyman continuum luminosity, as well as to the  $^{26}\text{Al}$  and  $^{60}\text{Fe}$  synthesis, the adoption of the total Lyman continuum luminosity should be preferred. The core-collapse supernovae, in fact, are dominated (in number) by the Type II supernovae whose range extends down to masses that contribute significantly to neither the Lyman continuum luminosity nor the  $^{26}\text{Al}$  nor the  $^{60}\text{Fe}$ . For example, the mass range 11–13  $M_{\odot}$  produces roughly 30% of the total number of Type II supernovae while their contribution to the synthesis of the  $^{26}\text{Al}$  is of the order of 6%; the situation would even worsen if the lower mass limit of the massive stars would reduce to 10 or even 9  $M_{\odot}$  because these stars would strongly affect the frequency of the Type II supernovae without contributing significantly neither to the Lyman continuum luminosity nor to the

$^{26}\text{Al}$  or to the  $^{60}\text{Fe}$  budgets. By normalizing to the total Lyman continuum luminosity estimated by Bennett et al. (1994) and an IMF slope  $x = 1.8$ , we predict roughly  $2 M_{\odot}$  of  $^{26}\text{Al}$  currently in the Galaxy in the NL00 case. The adoption of the LA89 models would reduce such an amount to  $1.7 M_{\odot}$ .

We have also fitted  $\gamma^2$  Velorum, the closest W-R star. In particular, we predict an abundance of  $5.82 \times 10^{-5} M_{\odot}$  of  $^{26}\text{Al}$  (for a  $60 M_{\odot}$ ), a value compatible with the current upper limit of  $6.3^{+2.1}_{-1.4} \times 10^{-5} M_{\odot}$ .

We did not address the fit to specific OB associations in this paper because it would require an evolutionary synthetic code,

as has been correctly addressed by, e.g., Cerviño et al. (2000), that is not available at present.

It is a pleasure to thank Roland Diehl and Nikos Prantzos for many helpful discussions. A. C. thanks his Institute, the IASF in Rome, and in particular the IBIS (INTEGRAL) group for continuous financial support. This research has been partially supported by the Ministry of the Education, University and Research (MIUR) through the grant PRIN-2004 (Prot. 2004029938).

## REFERENCES

- Anders, E., & Grevesse, N. 1989, *Geochim. Cosmochim. Acta*, 53, 197
- Angulo, C., et al. 1999, *Nucl. Phys. A*, 656, 3
- Arnett, W. D. 1977, *Ann. NY Acad. Sci.*, 302, 90
- Arnett, W. D., & Wefel, J. P. 1978, *ApJ*, 224, L139
- Arnould, M., Norgaard, H., Thielemann, F.-K., & Hillebrandt, W. 1980, *ApJ*, 237, 931
- Bao, Y. Z., Beer, H., Käppeler, F., Voss, F., Wisshak, K., & Rauscher, T. 2000, *At. Data Nucl. Data Tables*, 76, 70
- Bennett, C. L., et al. 1994, *ApJ*, 434, 587
- Caughlan, G. R., & Fowler, W. D. 1988, *At. Data Nucl. Data Tables*, 40, 283
- Cerviño, M., Knödseder, J., Schaerer, D., von Ballmoos, P., & Meynet, G. 2000, *A&A*, 363, 970
- Chieffi, A., & Limongi, M. 2002, *ApJ*, 577, 281
- . 2004, *ApJ*, 608, 405
- Chieffi, A., Limongi, M., & Straniero, O. 2000, *The Evolution of the Milky Way: Stars versus Clusters*, ed. F. Matteucci & F. Giovannelli (Dordrecht: Kluwer), 417
- Clayton, D. D. 1982, in *Essays in Nuclear Astrophysics*, ed. C. Barnes et al. (Cambridge: Cambridge Univ. Press), 401
- . 1984, *ApJ*, 280, 144
- Colella, P., & Woodward, P. R. 1984, *J. Comput. Phys.*, 54, 174
- Dearborn, D. S. P., & Blake, J. B. 1985, *ApJ*, 288, L21
- de Jager, C., Nieuwenhuijzen, H., & van der Hucht, K. A. 1988, *A&AS*, 72, 259
- Diehl, R., & Timmes, F. X. 1998, *PASP*, 110, 637
- Diehl, R., et al. 2006, *Nature*, 439, 45
- Formicola, A., et al. 2004, *Phys. Lett. B*, 591, 61
- Fuller, G. M., Fowler, W. A., & Newman, M. 1982, *ApJS*, 48, 279
- . 1985, *ApJ*, 293, 1
- Harris, M. J., et al. 2005, *A&A*, 433, L49
- Gupta, S. S., & Meyer, B. S. 2001, *Phys. Rev. C*, 64, 025805
- Iliadis, C., D'Auria, J. M., Starrfield, S., Thompson, W. J., & Wiescher, M. 2001, *ApJS*, 134, 151
- Jaeger, M., Kunz, R., Mayer, A., Hammer, J. W., Staudt, G., Kratz, K. L., & Pfeiffer, B. 2001, *Phys. Rev. Lett.*, 87, 202501
- Knödseder, J. 1999, *ApJ*, 510, 915
- Knödseder, J., et al. 1999, *A&A*, 344, 68
- Kroupa, P. 2004, *NewA Rev.*, 48, 47
- Kroupa, P., & Weidner, C. 2003, *ApJ*, 598, 1076
- Kunz, R., Fey, M., Jaeger, M., Mayer, A., Hammer, J. W., Staudt, G., Harissopulos, S., & Paradellis, T. 2002, *ApJ*, 567, 643
- Langanke, K. H., & Martínez-Pinedo, G. 2000, *Nucl. Phys. A*, 673, 481
- Langer, N. 1989, *A&A*, 220, 135
- Langer, N., Braun, H., & Fliegner, J. 1995, *Ap&SS*, 224, 275
- Leising, M. D., & Clayton, D. D. 1985, *ApJ*, 294, 591
- Limongi, M., & Chieffi, A. 2003, *ApJ*, 592, 404
- Mahoney, W. A., Ling, J. C., Jacobson, A. S., & Lingenfelter, R. E. 1982, *ApJ*, 262, 742
- Mahoney, W. A., Ling, J. C., Wheaton, W. A., & Jacobson, A. S. 1984, *ApJ*, 286, 578
- McKee, C. F., & Williams, J. P. 1997, *ApJ*, 476, 144
- Meynet, G., & Arnould, M. 1993, in *Nuclei in the Cosmos*, ed. F. Käppeler & K. Wisshak (Bristol: IOP), 487
- Meynet, G., Arnould, M., Prantzos, N., & Paulus, G. 1997, *A&A*, 320, 460
- Mowlavi, N., & Meynet, G. 2000, *A&A*, 361, 959
- Nugis, T., & Lamers, H. J. G. L. M. 2000, *A&A*, 360, 227
- Oberlack, U., et al. 2000, *A&A*, 353, 715
- Oda, T., Hino, M., Muto, K., Takahara, M., & Sato, K. 1994, *At. Data Nucl. Data Tables*, 56, 231
- Palacios, A., Meynet, G., Vuissoz, C., Knödseder, J., Schaerer, D., Cerviño, M., & Mowlavi, N. 2005, *A&A*, 429, 613
- Plüschke, S., et al. 2001, in *Exploring the Gamma-Ray Universe*, ed. A. Giménez & V. Reglero, V. (ESA SP-459; Noordwijk: ESA), 55
- Prantzos, N. 1989, *A&A*, 223, 136
- . 1991, in *AIP Conf. Proc. 232, Gamma-Ray Line Astrophysics*, ed. Ph. Durouchoux & N. Prantzos (Melville: AIP), 129
- . 2004 *A&A*, 420, 1033
- Prantzos, N., & Casse, M. 1986, *ApJ*, 307, 324
- Prantzos, N., de Loore, C., Doom, C., & Arnould, M. 1986a, in *Nucleosynthesis and its Implications on Nuclear and Particle Physics*, ed. J. Audouze & N. Mathieu (NATO ASI Conf. Ser. C, 163; Dordrecht: Reidel), 197
- Prantzos, N., & Diehl, R. 1996, *Phys. Rep.*, 267, 1
- Prantzos, N., Doom, C., de Loore, C., & Arnould, M. 1986b, *ApJ*, 304, 695
- Ramaty, R., & Lingenfelter, R. E. 1977, *ApJ*, 213, L5
- Rauscher, T., Heger, A., Hoffman, R. D., & Woosley, S. E. 2002, *ApJ*, 576, 323
- Rauscher, T., & Thielemann, F. K. 2000, *At. Data Nucl. Data Tables*, 75, 1
- Schaerer, D., & de Koter, A. 1997, *A&A*, 322, 598
- Smith, D. M. 2006, *NewA Rev.*, in press
- Takahashi, K., & Yokoi, K. 1987, *At. Data Nucl. Data Tables*, 36, 375
- Thielemann, F.-K., Nomoto, K., & Hashimoto, M.-A. 1996, *ApJ*, 460, 408
- Timmes, F. X., Woosley, S. E., Hartmann, D. H., Hoffman, R. D., Weaver, T. A., & Matteucci, F. 1995, *ApJ*, 449, 204
- Truran, J. W., & Cameron, A. G. W. 1978, *ApJ*, 219, 226
- Vink, J. S., de Koter, A., & Lamers, H. J. G. L. M. 2000, *A&A*, 362, 295
- . 2001, *A&A*, 369, 574
- Vuissoz, C., Meynet, G., Knödseder, J., Cerviño, M., Schaerer, D., Palacios, A., & Mowlavi, N. 2004, *NewA Rev.*, 48, 7
- Walter, R., & Maeder, A. 1989, *A&A*, 218, 123
- Ward, R. A., & Fowler, W. A. 1980, *ApJ*, 238, 266
- Weaver, T. A., & Woosley, S. E. 1993, *Phys. Rep.*, 227, 65
- Woosley, S. E., Langer, N., & Weaver, T. A. 1995, *ApJ*, 448, 315
- Woosley, S. E., & Weaver, T. A. 1980, *ApJ*, 238, 1017
- . 1995, *ApJS*, 101, 181 (WW95)